FMRP Regulates Neuronal RNA Granules Containing Stalled Ribosomes, Not Where Ribosomes Stall."

Jewel T-Y Li[1]; Mehdi Amiri[2,3], Senthilkumar Kailasam[4], Jingyu Sun[5,6], Nahum Sonenberg[2,3], Joaquin Ortega[5,6] and Wayne S. Sossin[1,*]

[1]*Department of Neurology and Neurosurgery, Montreal Neurological Institute, McGill University, Montreal, Quebec, Canada, H3A 2B4*

[2,]*Department of Biochemistry, McGill University, Montréal, QC H3A 1A3, Canada*

[3]*Goodman Cancer Institute, McGill University, Montréal, QC H3A 1A3, Canada*

[4]*Canadian Centre for Computational Genomics, McGill University, Montreal, Quebec H3A 0G1,* Canada

[5]Department of Anatomy and Cell Biology, McGill University, Montreal, Quebec H3A 0C7, Canada.

[6]Centre de Recherche en Biologie Structurale, McGill University, 3649 Promenade Sir William Osler, Montreal, Quebec H3G 0B1, Canada.

*Correspondence. Wayne.sossin@mcgill,ca

Abstract

Local protein synthesis is a crucial process that maintains synaptic proteostasis. A large percentage of mRNAs translated in developing neurons are associated with stalled ribosomes. FMRP, the protein lost in Fragile X syndrome, is highly enriched in RNA granules that contain stalled ribosomes. Previous examination of ribosome protected fragments (RPFs) from stalled neuronal ribosomes has identified motifs that match those found in mRNAs associated with FMRP, as recognized by FMRP cross-linking immunoprecipitation (CLIP) (Anadolu et al, 2023, Journal of Neuroscience doi: 10.1523/JNEUROSCI.1002-22.2023). To investigate whether FMRP recognition of these sequences is important for determining where ribosomes are stalled on mRNAs, we examined stalled ribosomes RPFs isolated from P5 mice of both sexes lacking the FMRP protein. We found that the loss of FMRP had no effect on the proteins associated with neuronal stalled ribosomes, the structure of the ribosomes, or the stalling sites (locations where RPFs accumulated). However, we observed a significant decrease in the amount of mRNAs previously shown to be associated with FMRP by CLIP in stalled ribosomes. Additionally, the number of neuronal RNA granules containing stalled ribosomes, as assayed by ribopuromycylation in distal neurites, decreased. Unlike neuronal RNA granules in WT neurons, the remaining distal neuronal RNA granules were resistant to reactivation by stimuli that induce mGLuR-LTD. These results highlight important roles of FMRP in regulating neuronal RNA granules that contain stalled ribosomes, though it does not influence where ribosomes are stalled and is not directly involved in stalled ribosome formation.

Introduction

Neurons are structurally unique cells with synapses–sites where neurons connect with each other– often located far from the cell body. For example, hippocampal pyramidal dendrites span an average of 13.5 mm (Ishizuka et al., 1995) while axonal tips can extend up to a meter away from the cell body (Debanne et al., 2011). To maintain and adapt the local proteome in response to local neuronal activity, neurons rely on the ability to produce proteins locally. Indeed, local protein synthesis has been shown to be critical for many aspects of neuronal function including growth cone guidance (Yoon et al., 2009), homeostasis (Holt et al., 2019), aspects of presynaptic firing (Wong et al., 2024) and certain forms of synaptic plasticity (Holt et al., 2019)

Local protein synthesis relies on coordinated mechanisms that couple mRNA transport with translational repression. Two major mechanisms have been proposed to regulate this process in neurons (Kiebler and Bassell, 2006; Sossin and DesGroseillers, 2006). In one mechanism, mRNAs are stalled during initiation and transported within RNA transport particles. In this case, the completion of initiation and onset of elongation depends on removal of the repression mechanisms and availability of ribosomes, which must be transported separately. In contrast, mRNAs can be transported along with ribosomes if elongation is stalled, with stalled ribosomes serving as the transport unit. Both mechanisms are likely to be utilized for neurons. While RNA transport particles appear to facilitate transport of individual mRNAs (Batish et al., 2012), stalled ribosomes are found within large RNA granules that appear to contain multiple different mRNAs (Langille et al., 2019). The RNA binding protein (RBP) FMRP has been implicated in both types of transport (Richter et al., 2015).

Loss of FMRP causes Fragile X syndrome. In humans, the loss of FMRP occurs due to the expansion of a CGG repeat in the 5' untranslated region (UTR) of the gene, leading to excessive methylation and transcriptional inhibition. Since CGG expansion is relatively common compared to de novo mutations and the gene is X-linked, Fragile X syndrome is a relatively common neurodevelopmental disorder and is the leading genetic cause of autism (Yu and Berry-Kravis, 2014). FMRP is an RBP and thus plays a role in various aspects of RNA biology. Several of these functions have been implicated in Fragile X syndrome, including FMRP's regulation of miRNA repression, splicing, translation initiation, and translational elongation (Richter et al., 2015; Richter and Zhao, 2021). Another proposed cause of Fragile X syndrome are interactions between FMRP and proteins independent of RNA binding, including the direct regulation of ion channels (Deng and Klyachko, 2021).

A common finding in models of Fragile X is that the loss of FMRP increases translation (Huber et al., 2002; Qin et al., 2005). This increase may result from the direct effects of FMRP on translation initiation or elongation, or from the loss of specific FMRP targets, which in turn lead to changes in signal transduction that ultimately result in increased protein synthesis (Bagni and Zukin, 2019). A major finding regarding how FMRP regulates translation is that, unlike most RBPs, FMRP exhibits strong association with the coding region in cross-linking immunoprecipitation (CLIP) studies, implicating FMRP in stalling elongation (Darnell et al., 2011). Consistent with a role in ribosomal stalling, loss of FMRP caused shifts in polysome profiles of CLIP-identified FMRP targets in Neuro2A translational extracts (Darnell et al., 2011). Additionally, elongation rates are also increased in mouse models of FMRP, where FMRP is

knocked out (Udagawa et al., 2013). While initially studies suggested that FMRP associates non-discriminately throughout the coding region, more comprehensive bioinformatic analyses have revealed consensus sequences that were enriched in FMRP CLIP data (Ascano et al., 2012; Anderson et al., 2016). FMRP has also been shown to bind to specific motifs such as G quadruplexes and the Kissing complex due to specificity of the RNA binding domains in the protein (Darnell et al., 2005), but the sequences enriched in FMRP CLIP data do not necessarily contain these motifs (Anderson et al., 2016).

Ribosomes from neuronal RNA granules have been enriched through sedimentation and biochemically and structurally characterized (Krichevsky and Kosik, 2001; Elvira et al., 2006; El Fatimy et al., 2016; Kipper et al., 2022; Anadolu et al., 2023). These ribosomes are stalled in the hybrid state (Kipper et al., 2022; Anadolu et al., 2023) and may possess other modifications that distinguish them from most ribosomes: For example, unlike most ribosomes, puromycylated peptides do not dissociate from neuronal stalled ribosomes (Anadolu et al., 2024). Additionally, anisomycin competes poorly with puromycin for puromycylation, a property not observed in most ribosomes (Anadolu et al., 2024). Examination of RPFs from these ribosomes have also shown differences from standard preparations: the protected fragments are larger than expected, >35 as opposed to 28 or 32; there is enrichment for the RPFs to encode glutamic acid and aspartic acid, and the motifs previously identified in FMRP CLIPs are enriched in the RPF sequences (Anadolu et al., 2023). It is not clear whether the enrichment of FMRP CLIP-associated sequences in RPFs from stalled ribosomes occurs because FMRP determines where ribosomes stall, or whether FMRP associates with stalled ribosomes that were already paused at these specific sequences.

To determine whether FMRP is directly involved in the formation of stalled ribosomes through sequence recognition, we compared RPFs from stalled ribosomes in mice lacking FMRP protein to those in WT mice of the same strain. We also tested whether the larger protected fragments could be reduced in size by higher nuclease treatment. Our findings show stronger nuclease treatment does reduce the size of RFPs to the normal size. Despite its enrichment in RNA granules containing stalled ribosomes FMRP does not appear to be important for the formation of stalled ribosomes since the loss of FMRP did not affect the association of other proteins with stalled ribosomes, the state of the stalled ribosomes, and, most importantly, where the ribosomes stalls. However, using ribopuromyclation to detect RNA granules containing stalled ribosomes, we found that the loss of FMRP decreased the number of distal RNA granules. This suggests that FMRP plays a crucial role in stabilizing distal RNA granules and regulating their controlled reactivation.

Results

Comparing RNA Binding Protein enrichment in WT and FMR1-KO RNA Granules

Stalled ribosomes are found in neuronal RNA Granules (Graber et al., 2013). Previous studies have demonstrated that stalled ribosomes from RNA granules sediment in sucrose gradients used to separate monosomes from polysomes (Krichevsky and Kosik, 2001; Aschrafi et al., 2005; Elvira et al., 2006). This sedimentation was further optimized to separate the ribosomes from RNA granules from heavy polysomes (El Fatimy et al., 2016; Anadolu et al., 2023). To compare mouse and rat brain preparations, we collected three fractions: the starting material, fractions 5/6, and the pellet, which we refer to as the RNA granule fraction (RG). (Fig. 1A). While fraction 5/6 is usually referred to as the polysome fraction (El Fatimy et al., 2016; Anadolu et al., 2023), due to its structural similarity to RNA Granules (Anadolu et al., 2023) we conservatively call them ribosome clusters (RC). To determine whether the RG fraction enriched from C57BL-6 mice is comparable to the ones extracted from rat brains in a previous study (Anadolu et al., 2023), we examined the protein distribution across all collected fractions from each species' brain homogenate using Coomassie blue staining. The protein distribution was similar between rat brain and WT mouse brain with considerable amounts of proteins in both WT-mouse RG and rat RG (Fig 1B). We further confirmed WT-mouse RG and rat RG were comparable to each other through immunoblotting WT mouse preparations with key proteins from previous study such as FMRP and eEF2 (Anadolu et al., 2023). Similar to previous results from rat RG, WT mouse RG was enriched in FMRP compared to the RC and starter fraction, whereas eEF2 was not detectable in either the RC or RG (Fig. 1C). Overall, these findings indicate that the WT-mouse

brain RG is similar to rat brain RG, allowing us to use WT-mouse to further study stalled ribosomes from neuronal RNA Granules.

To analyze the effect of FMRP, we examined the RG and RC from FMR1 knockout mice (FMR1-KO). FMR1-KO mice is the most common model for studying FMRP's function and Fragile X Syndrome (Richter and Zhao, 2021). We confirmed that FMRP is knocked out (Fig 1C). In addition, we compared the level of ribosomes in the RG and the RC normalized to starting material (Fig. 1D). If FMRP was critical for the formation of RNA Granules, there should be fewer ribosomes in the RG compared to the RC without FMRP. Instead, we observed an increase in the relative levels of ribosomes (assessed using immunoblotting to the ribosomal protein S6) in FMR1-KO (Fig. 1H). All subsequent results are normalized to the levels of S6 to obtain the levels of RNA binding protein (RBPs) relative to the ribosomes in the RG and the RC.

To investigate the loss of FMRP on stalled ribosomes, we looked at two key proteins that are essential for stalled ribosomes formation-UPF1 and Stau2 (Graber et al., 2017). There were no differences in enrichment for UPF1 and Stau 2 isoforms (Duchaine et al., 2000) between WT and FMR1-KO (Fig 1C-K). Thus, while there appear to be more ribosomes in RGs compared to RCs in FMRP mice, the overall granule composition is similar.

Anisomycin and Puromycin Competition indicates the similarity in WT and FMR1-KO RNA Granules

Previous cryo-EM studies of ribosomes isolated from RNA granules showed that most ribosomes found in RNA Granules are in the hybrid A/P and P/E configuration (Kipper et al., 2022; Anadolu et al., 2023). Puromycin and anisomycin are both translational inhibitors that bind to the A site of the ribosomes (Hansen et al., 2003; Garreau de Loubresse et al., 2014). Due to their overlapping binding sites, anisomycin inhibits puromycin from binding to the ribosomes when both are present. However, we previously showed that puromycylation of neuronal ribosomes in cell culture and puromycylation of ribosomes sedimented from neuronal RNA Granules are resistant to anisomycin inhibition (Anadolu et al., 2024). This suggested that the binding site for these translational inhibitors is altered in the neuronal stalled ribosome, either due to the enrichment of the hybrid state, or due to other differences in these ribosomes. Thus, by looking at the percentage of puromycylation present in the presence of anisomycin, we can estimate the number of ribosomes in this state.

We performed these experiments on the ribosomes that were sedimented through the sucrose gradient (Fig 2A). We first validated that puromycylation in non-neuronal ribosomes, in this case- rat liver ribosomes, were not resistant to anisomycin. Indeed, we saw a total inhibition of puromycylation by anisomycin in sedimented rat liver ribosomes (Fig 2B) much like the effect previously seen on HEK cell culture (Anadolu et al., 2024). This indicated that neither homogenization in our buffer nor high centrifugation is sufficient to cause puromycin's resistance to anisomycin and further confirmed the neuronal specificity of this ribosomal state. We next examined if WT and FMR1-KO RG exhibit the same level of puromycylation in the presence of anisomycin. We found that the WT and FMR1-KO were comparable to each other

(2C, 2D). Thus, FMRP does not seem to be important for the formation of this state of the ribosome.

Effects of Digestion and Mg^{2+} on ribosome structure and RPF size in RNA Granules

To explore if the stalling sites of the ribosomes are altered by the loss of FMRP, we examined RPFs (Fig. 3A). RPFs generated from the rat RG were generally above 35nt (Anadolu et al., 2023), while the RPF has a canonical size between 28nt and 32nt (Ingolia, 2014). It was unclear whether the extension at the 3' end from the RPF generated from rat RG was due to an extended conformation of the ribosome to protect a larger fragment or due to altered nuclease resistance in this region (Anadolu et al., 2023). Thus, we investigated whether this extended region could be cleaved off with more effective nuclease treatment. To determine if the extending nucleotides could be removed by increasing the effectiveness of nucleases, we digested in room temperature instead of 4°C, and in addition, the 1µl RNAse digestion was adjusted to the concentration of the RC or RG (see Methods).

We replicated the increased size of RPFs in mice using the old protocol, however, RPFs generated from high nuclease treatment decreased the RPFs to around 28nt (Fig 3B). While there was still a portion of RPFs that stayed around 35 nt (Fig 3B), the majority of these mRNA are noncoding mRNAs (Extended Data Table S3-1). The high nuclease treatment also displayed a higher percentage of RPFs in the coding region (CDS) (Fig 3C) and a higher periodicity (Fig. 3D, E). These results were consistent across RC, RG, WT and FMR1-KO (Fig. S3-1, S3-2, S 3-3).

An additional change from the previous protocol was in the concentration of $MgCl_2$. The previous solution used to extract the ribosomes (20mM Tris-HCl, ph7.4; 150mM NaCl; 2.5 mM $MgCl_2$) has cellular levels of Mg^{2+}. A cryo-electron microscopy (cryo-EM) characterization of RNase I-treated RG purified under this low magnesium concentration (Anadolu et al., 2023) found that 85% of the ribosomes contained in the RG exhibited tRNA molecules in hybrid A/P and P/E state. The remaining 15% of the ribosome population in this sample contained a tRNA in the P/P state. To test whether increasing the magnesium concentration had any effect on the percentage of ribosomes in hybrid A/P and P/E state, we repeated the cryo-EM and image classification analysis (Fig. S4-1) after the purification was performed in a buffer containing 20mM Tris-HCl, ph 7.4; 150 mM NaCl; 10 mM $MgCl^{2+}$. We found that high Mg^{2+} did not impact the percentages of hybrid A/P and P/E state (83%) and P/P (17%) state ribosomes (Fig. 4A). The cryo-EM maps for the hybrid and P/P state ribosomes were refined to 2.8 Å and 3.2 Å, respectively (Fig. S4-2 and Table S4-1).

We also performed DEG analysis to examine differences between the RPFs generated from the RG from the high nuclease, high magnesium protocol (M protocol) and the RPFs extracted from the RG with the low nuclease, cellular magnesium concentratin protocol (Extended Data Table S4-1). GO Analysis of the significant genes generated from the DEG analysis revealed that the RPFs from the M protocol has less mRNAs processed through the secretory pathway (Extended Data Table S4-1; Fig 4B). In other words, high Mg^{2+} decreased the abundance of mRNAs normally co-translationally inserted into the ER which are unlikely to be components of

transporting RNA granules containing stalled ribosomes and solidified our focus on the M protocol in the analyses below.

Characterization of the RPFs of mRNAs in the WT and FMR1-KO RNA Granules through DEG and GO Analysis

To analyze the mRNAs in the WT and FMR1-KO RNA Granules, we mapped the RPFs to its corresponding mRNAs (Fig. 5A), similar to our previous analysis of RFPs from rat RNA granules (Anadolu et al., 2023). To compare the samples across different biological preparations, we calculated for the reads per kilobase per million mapped reads (RPKM), which normalized the mRNA count against the total mapped count and gene length (Extended Data Table 5-1). The number of RPFs/mRNA normalized against total mRNA obtained from whole brain homogenate with RNA-SEQ, often termed translational efficiency, was also calculated in the RGs (Extended Data Table 5-1). Here we referred to this term as ribosomal occupancy since the subject of this study is stalled ribosomes and is unlikely to be related to active translation. While the loss of FMRP has led to significant changes in mRNA levels in other studies (Thomson et al., 2017; Sawicka et al., 2019; Kurosaki et al., 2022; Ntoulas et al., 2024) we observed very few differences in RNA-SEQ between control and FMRP from whole P5 brains (Extended Data Table 5-2). Lastly, we calculated for enrichment between RG and RC to determine the groups of mRNAs that are selected into the RG fraction (Extended Data Table 5-1).

When comparing GO Analysis to identify which groups of mRNAs dominated the WT and FMR1-KO RG, we did not see considerable differences. The GO Analysis on the top 500 abundant mRNAs in the WT RG and FMR1-KO RG showed cytoskeleton encoding mRNAs to

be the most abundant (Fig 5B; Extended Data Table 5-3). This matched with the previous result from rat RG (Anadolu et al., 2023). For occupancy in RG, GO Analysis revealed WT and FMR1-KO RG still were most occupied by cytoskeleton related mRNAs, such as microtubule, microfilament, actin filament (Fig 5B; Extended Data Table 5-3). In addition, both WT and FMR1-KO RG were highly occupied in mRNA processing, like splicing and RNA localization (Fig 5B). This also replicated the previous result from rat RG (Anadolu et al., 2023). We also accessed the most enriched mRNAs in WT and FMR1-KO RG. We found that much like abundance, occupancy, the WT and FMR1-KO RG are both highly enriched in mRNAs encoding cytoskeletal proteins (Fig. 5B).

We next compared the specific effects of FMRP on RG by performing DEG Analysis on FMR1-KO and WT on RG abundance, occupancy, and enrichment. There were only 2 protein coding genes that were significantly different between the abundance of FMR1-KO and WT in protein coding genes – FMR1 and Wdfy1 (Extended Data Table 5-2). There were no significantly different genes between WT and FMR1-KO occupancy and enrichment. Thus, no difference rose to significance, given the large number of mRNAs used in this analysis.

Comparison of the ribosome protected fragments of mRNA in the WT and FMR1-KO to selected datasets

Previously, we showed that specific subsets of mRNAs are enriched in the RG fraction (Anadolu et al., 2023). We first examined the number of mRNAs that are associated with ribosomes resistant to ribosome runoff (Shah et al., 2020) (Extended Data Table 6-1). Similar to previous

experiments with rats, the most abundant mRNAs resistant to run off were significantly abundant, occupied and enriched in both WT and FMRP RPFs (Fig 6). Thus, loss of FMRP did not affect the enrichment of mRNAs that were independently shown to make up the most abundant mRNAs remaining on ribosomes after run-off (i.e. mRNAs stalled in elongation). Next, we investigated FMRP associated mRNAs through assessing FMRP-Clipped mRNAs in WT and FMR1-KO GF (Darnell et al., 2011; Maurin et al., 2018) (Extended Data Table 6-1). These mRNAs had been identified by cross-linking FMRP with mRNA, fragmenting the mRNA, immunoprecipitating the mRNA still associated with FMRP and sequencing this mRNA. We found that FMRP-Clipped mRNAs were highly abundant, enriched and occupied in WT RG (Fig 6A, Fig 6C, Fig 6E), which replicated the previous results obtained from rat RG (Anadolu et al., 2023). Interestingly, while still significant, there appeared to be a decrease in the relative abundance of these mRNAs in the FMR1-KO (Fig 6B) and particularly, the mRNAs identified in the Darnell study did not show a significant increase in occupancy compared to all mRNAs (Fig 6D). However, the FMRP clipped mRNAs were still highly enriched in the RG compared to RC, for both WT and FMR1-KO (Fig 6E, F). We next examined the specific effect of FMRP on these subsets of mRNA by calculating the fold change in abundance, occupancy, and enrichment of these specific mRNAs between WT and FMR1-KO RG and compared them to changes in all mRNAs (Extended Data Table 7-1). The loss of FMRP significantly affected the abundance and occupancy of FMRP-Clipped mRNAs in WT and FMR1-KO RG (Fig 7A, 7B), but not their enrichment between RG and RCs (Fig 7C). This was because the abundance of these mRNAs in the RCs was also reduced (Fig 7D). In contrast, there was no effect of the loss of FMRP on the abundance and occupancy of mRNAs related to ribosomes resistant to run-off suggesting that

overall stalled mRNAs were not affected, just mRNAs that were associated with FMRP (Fig 7A, 7B). It should be noted that the difference in abundance and occupancy of FMRP-clipped mRNAs in the FMR1-KO were relatively small and only significant when looked at in the whole subset. Individual mRNAs in this group were not found to be significantly different in the DEG analysis (Extended Data Table 5-2).

Peak Analysis on the WT and FMR1-KO RNA Granules

The distribution of RPFs in stalled ribosomes is dominated by peaks, presumably representing stalling sites. Our previous result showed that RPFs in the peaks from the RG fraction were enriched with FMRP related mRNA motifs (Anadolu et al., 2023). Thus, to inquire if the loss of FMRP altered the location of stalled ribosomes, peaks were identified in each of the six RG preparations (3 WT and 3 FMR1-KO) (Fig. 8A)

We identified 1392 peaks that were present in all six samples. In contrast, there were many fewer peaks solely present in WT or solely FMR1-KO: 317 peaks for WT and 225 peaks for FMR1-KO (Extended Data Table 8-1; Fig. 8B). This implied a high overlap in the location of peaks between the WT and FMR1-KO RPFs. In general, the distribution of RPF peaks is quite similar in different biological preparations, as exemplified by the Tubb2b mRNAs (Fig. 8C), a cytoskeletal mRNA that shows high ribosomal occupancy in our samples and was also examined in the previous manuscript (Anadolu et al., 2023).

Moreover, similar to our previous results, the majority of peaks contain a FMRP related motif, and this was not different in the peaks that were enriched in all the samples and the peaks that were only identified in the WT (i.e not seen in FMR1-KO mice) or only in FMR1-KO mice

(i.e. not seen in WT mice) (Figure 8B). Previously, we found that these peaks were enriched in negatively charged amino acids, glutamic acid and aspartic acid. This was also true for the peaks here, regardless of whether they were present or absent in the FMR1-KO mice (Fig. 8B).

To rule out that peaks were due to amplification artifacts in the preparation of RPFs we repeated these analyses after removing PCR duplicates (Fig. S8-1; Extended Data Table S8-3) and found over 95% of the peaks identified without removing PCR duplicates were defined as a peak in at least one of the biological replicates after removing duplicates. More importantly, we found similar results with enrichment of FXS motif and enrichment of negative charged amino acids in the FMR1-KO only, WT only and both peaks (Fig. S8-1; Extended Data Table S8-3) after removing PCR duplicates.

Loss of FMRP decreases distal RNA granules containing stalled ribosomes.

Since FMRP did not appear to affect the location on mRNAs where the ribosomes were stalled, we next examined the size, number and location of neuronal RNA granules containing stalled ribosomes in WT and FMR1-KO hippocampal culture (Fig. 9A). FMRP is localized to neuronal RNA granules in hippocampal neuronal cultures (Graber et al., 2013; El Fatimy et al., 2016). We examine neuronal RNA granules containing stalled ribosomes in hippocampal neurons using a technique called ribopuromycylation (RPM)(David et al., 2013). The ribosomes covalently link puromycin to nascent peptide chains on ribosomes in a process called puromycylation. It was proposed that emetine could prevent the puromycylated nascent chains from diffusing away from the ribosome and thus allow localization of ribosomes with nascent chains using immunohistochemistry with antibodies to puromycin (David et al., 2013). RPM in neuronal

cultures revealed large puncta in neurites that were insensitive to run-off by the homoharringtonine (HHT, an inhibitor that allows run-off of translating ribosomes, but prevents the first step of elongation), suggesting that these large puncta are RNA granules containing stalled ribosomes (Graber et al., 2013). Later, other studies suggested that emetine was not sufficient in most cases to retain puromycylated nascent chains on ribosomes (Enam et al., 2020; Hobson et al., 2020). However, we found that puromycylated nascent chains are retained on neuronal stalled ribosomes, even in the absence of emetine, perhaps due to a peptide-mediated ribosomal stall (Anadolu et al., 2024). Thus, RPM is still appropriate to localize stalled ribosomes in neurons.

We found that the number of large RPM puncta (>0.15 square microns) in distal neurites (>50 microns from the cell soma) was significantly decreased in hippocampal cultures from mice lacking FMRP (Fig 9A, 9C). There were no differences in the average size of the remaining puncta (Fig. 9D) and the RPM puncta were equally resistant to both run-off with HHT and anisomycin (Fig. S9-1) consistent with these puncta representing large collections of neuronal stalled ribosomes. Previously we have shown that DHPG can decrease the number of distal RMP puncta in these cultures, correlated with the reactivation of translation from stalled ribosomes (Graber et al., 2013; Graber et al., 2017). We replicated this result, DHPG significantly decreased the number of distal RPM puncta in WT cultures, but DHPG had no significant effect on the decreased number of puncta in cultures from FMRP lacking mice (Fig. 9B,C). This is consistent with a loss of distal DHPG-sensitive RPM puncta in the absence of FMRP.

Discussion

Overall, there appeared to be no major changes in the biochemical composition of stalled ribosomes in the absence of FMRP (Fig. 1) or the state of the stalled ribosomes (Fig. 2). Most importantly, the places where ribosomes stall (peaks) are not changed in the absence of FMRP. The majority of peaks observed overlapped in both WT and FMR1-KO mice, and FMR1-KO RPFs still contained motifs in mRNAs previously shown to associate with FMRP (Fig. 8). Thus, the major conclusion of our study is that FMRP does not affect the locations at which neuronal ribosomes stall.

We did not observe major changes in RNA Seq between control and FMR1-KO in P5 brains. This differs from many studies that do show differences in RNA-Seq between these two groups at other stages of development, or not examining the whole brain (Thomson et al., 2017; Sawicka et al., 2019; Kurosaki et al., 2022; Ntoulas et al., 2024). It is likely that our use of whole brains, a specific time point, and relatively small number of biological replicates decreased our ability to see FMRP-related changes in mRNAs that are observed at a more cell-type specific level and at different developmental times. This may also be true for our lack of changes at the RPF level from stalled ribosomes. Nevertheless, if FMRP binding was the critical determinant for presence in neuronal RNA granules, we would have expected to observe more differences.

There were subtle changes in the mRNAs present in the RCs and RGs in the absence of FMRP. Most importantly, if we focused just on the mRNAs identified in FMRP Clips, there was a decrease in the relative abundance and occupancy of these mRNAs in both RGs and RCs. It appears that in the absence of FMRP there is less ribosomal occupancy of mRNAs in both

fractions. This is consistent with a role of FMRP in initiation as only initiated mRNAs can be stalled or found in the RC and RG fractions. Indeed, there is considerable evidence that FMRP regulates initiation of a subset of mRNAs (Santini and Klann, 2014; Bagni and Zukin, 2019). It is possible that FMRP is more associated with ribosomes on mRNAs that they helped initiate .

Our finding suggests that FMRP does play important roles for stalled ribosomes. Loss of FMRP led to a decrease in RPM distal puncta and the remaining puncta were insensitive to DHPG (Fig. 9). One possibility is that FMRP serves as a stabilizer for the RNA granules and must be removed before reactivation. FMRP contains RGG low complexity domain that allows phase separation to form spontaneously (Zhang et al., 2022). This may explain how FMRP is associated with the liquid-liquid phase separated granules in neurites (Anadolu and Sossin, 2020). FMRP is subjugated to post translational modification by neuronal stimulus such as mGluR-LTD (Niere et al., 2012; Khayachi et al., 2018) that reactivates translation from stalled ribosomes (Graber et al., 2013; Graber et al., 2017). Loss of FMRP also leads to an increase in the amount of mGLUR-LTD and removes the protein synthesis requirement for mGLUR-LTD (Hou et al., 2006; Nosyreva and Huber, 2006). These findings support a model in which FMRP plays a key role in retaining stalled ribosomes within RNA granules by maintaining their liquid-liquid phase, while post-translational modifications of FMRP regulate the controlled disassembly of these granules, enabling translational reactivation. In the absence of FMRP, spontaneous loss of the liquid-liquid phase may be more frequent leading to premature reactivation of stalled ribosomes and thus a loss of distal RNA granules and premature production of proteins from mRNAs stalled in RNA granules.

An inconsistency in our findings is the loss of distal RPM puncta coupled with an increase in the immunoreactivity for S6 in the RG fraction from rat P5 brains. While clusters of stalled ribosomes are enriched in the pellet, it is not clear that only stalled ribosomes in neuronal RNA granules are present in the RG pellet. In hippocampal cultures, a high fraction of nascent chains are present in stalled ribosomes but the majority of RPM staining is in the soma and proximal neurites, not in distal granules (Graber et al., 2013; Graber et al., 2017; Langille et al., 2019). Thus, it is likely that the RG fraction is not simply made up of ribosomal clusters from the large liquid-liquid phase RNA granules. It is likely that a proportion of the stalled ribosomes are not stored in large RNA granules, but still pellet in the sucrose gradients. This fraction may be greater in the absence of FMRP.

Our previous results showed a larger protected fragment in RNA granules, but here we showed that this was due to incomplete nuclease protection. This incomplete digest was much more obvious at the entry site of the ribosome, than at the exit site, as the difference is cleavage is mainly at the 3'end of the protected mRNA (Anadolu et al., 2023)(Fig. 3). It is still unclear where this is due to increased nuclease resistance of the mRNA near the entrance site of the ribo some in stalled ribosomes due to secondary structures or just differences in nuclease accessibility to the region near the entrance site that is not neuronal specific. Further research on the mechanism of stalling may make this clearer.

There was a decrease in the presence of secretory mRNAs in the RG fraction due to the increased Mg^{2+} concentration in the buffer (Fig. 4). Ribosomes containing secretory mRNA are stalled by the signal recognition protein and then co-translationally inserted into the ER. If these

ribosomes were transported in a stalled state, they would presumably have to be co-transported with the secretase and ER membranes. There is considerable evidence that some local mRNAs hitchhike with mitochondria or endosomes (Fernandopulle et al., 2021), but so far, evidence for co-transport of ER with mRNAs, particularly in RNA granules, is lacking. We think it is more likely that sedimentation enriches mRNAs encoding secretory proteins as a contamination and that, for reasons that are still unclear, higher Mg^{2+} concentrations during sedimentation reduce this contamination. Nevertheless, it will be interesting in the future to examine whether secretory mRNAs with high ribosomal occupancy in the RG fraction are indeed associated with ER and whether there are ER fragments in neuronal RNA granules.

Conclusions

We previously showed that the peaks of RPFs in stalled ribosomes contain sequences enriched in FMRP CLIPped experiments (Anadolu et al., 2023). Here we show that this is independent of FMRP since the enrichment of FMRP-CLIPped sequences is observed even when FMRP is lost. This suggests that instead of FMRP driving the recognition of the stalling sites, the sequences may direct the stalling of ribosomes and FMRP associates with stalled ribosomes. Moreover, FMRP does not play a role in the distinct conformational change of neuronal stalled ribosomes as it did not affect their anisomycin-resistant puromycylation, not does it alter the proteins associated with stalled ribosomes. FMRP does play a role in distal RNA granules containing stalled ribosomes since their number is decreased in the absence of FMRP, and the remaining granules are not reactivated by DHPG.. We propose that FMRP is important for the

regulated dissociation of the liquid-liquid phase RNA granules and that this is an important step in the normal reactivation of neuronal RNA granules.

Methods

Purification of the RNA Granule-Enriched Fraction

All preparations used brains that were flashed frozen using either liquid nitrogen or ethanol dry ice bath after dissection. Either five rat brains (Sprague Dawley; Charles Rive Laboratory) or 10 mouse brains (C57Bl/6) from WT and FMR1-KO mouse were used. Samples were homogenized in either the previous (Anadolu et al, 2023) RNA Granule Buffer (20 mM Tris-HCl pH 7.4 (catalog #BP152-1, Thermo Fisher Scientific), 150 mM NaCl (catalog # BP358-212, Thermo Fisher Scientific), 2.5 mM $MgCl_2$ (catalog# M33-500, Thermo Fisher Scientific)) or high Mg2+ RNA Granule Buffer (20 mM Tris-HCl pH 7.4, 150 mM NaCl, 10 mM MgCl2. These buffers were supplemented with 1 mM DTT (catalog #D9163, Sigma-Aldrich), and 1 mM EGTA (catalog # E8145 Sigma-Aldrich) for homogenization. The homogenate was centrifuged 15min in a Thermo Fisher Scientific T865 fixed-angle rotor at 6117 x g at 4°C to separate debris, such as lipid and extracellular matrix, from the ribosomes. The supernatant was collected with some set aside as starter fraction. The rest of the supernatant was then clarified with 1% iGEPAL CA-630 (catalog #04693132001, Roche) for 5 min at 4 C. Sucrose solution was produced by suspending sucrose (catalog #8550, Calbiochem) with RNA Granule buffer. The samples were loaded onto a 60% sucrose pad in a Sorvall 36 ml tube (Kendro, catalog #3141, Thermo Fisher Scientific) and centrifuged at 56,660 x g for two hours in AH-629 swing-bucket rotor to retrieve the ribosomes. The ribosomes were resuspended in RNA Granule buffer then reloaded onto 15%-60% sucrose gradient and centrifuged at 56,660 xg for 45 min to separate the ribosomes

into monosomes, ribosomal clusters (RC) and RNA Granule (RG). Each fraction was 3.5 ml and collected from the top. We retrieved RCs from fraction 5 and 6, RNA Granules from the pellet.

Immunoblotting and quantification of enrichment

For Immunoblotting, the RG and RC were ethanol precipitated and resuspended with 1x sample buffer and Granule buffer. The samples were loaded onto 10%, 12% or 15% acrylamide gel according to the observing protein sizes. The gel was either stained with Coomassie Brilliant Blue to look at the protein distribution or transferred onto a 0.45um nitrocellulose membrane (catalog #1620115, Bio-Rad) for immunoblotting. The transferred membranes were stained with Ponceau and imaged. Then, the membranes were blocked with 5% BSA (catalog # A9647, Sigma Aldrich) in Tris-buffered saline with Tween before incubation with primary antibodies—rabbit anti-s6 (1:10,000) (catalog #2217, Cell Signaling Technology), rabbit anti-FMRP (1:500)(catalog #4317, Cell Signaling Technology), rabbit anti-UPF1 (1:10,000)(catalog #ab133564, Abcam), mouse anti-Stau2 (1:1000)(catalog #MM0037-P, MediMabs), anti-eEF2 (1:1000)(catalog #2332S, Cell Signaling Technology), rabbit anti-Pur-alpha (1:1000)(catalog #ab79936, Abcam), and anti-mouse puromycin (1:1000)(catalog #ab2619605, Developmental Studies Hybridoma Bank). Membranes were washed with TBS-T after incubation. HRP-conjugated secondary antibodies such as anti-rabbit HRP (1:10,000)(catalog #31460, Thermo Fisher Scientific) and anti-mouse HRP (1:10,000)(catalog #31430, Thermo Fisher Scientific) were incubated with the membranes for detection. ECL reaction was performed for imaging, and the images were scanned and quantified by ImageJ software. The single band for each protein was selected and quantified using ImageJ's Gel analysis Macro. For S6, the levels in the RG and

RC were normalized against S6 signal intensity in the starter. For other proteins, the levels in starter, RC and RG were divided by S6 levels in that fraction, and the RC and RG values were normalized to the ratio in the starter fraction. The enrichment between the RC and RG was calculated by RG divided by RC. A two tailed, unequal variance t-test was performed between the enrichment of WT and FMR1-KO to observe the differences between the two groups. Data was graphed via excel.

Inhibition of Puromycylation by Anisomycin

The liver ribosomes were extracted from P5 Spraque Dawley rats were retrieved and extracted through the identical method as the RNA Granules, but without the last spin since liver does not contain RNA Granules. All ribosomal fractions used were incubated for 5 min in 1) RNA Granule buffer 2) 100µM puromycin (catalog# P7255, Sigma Aldrich), or 3) 100µM puromycin and 100µM anisomycin (catalog# A9789, Sigma Aldrich). The samples were then ethanol precipitated, immunoblotted and quantified via the method stated above. The percentage of puromycin resistant to anisomycin inhibition were calculated by dividing anti-puro signal from the puromycin and anisomycin added sample against the anti-puro signal from the puromycylated sample within each replicate.

Digestion and extraction of the monosomes

The RC samples were loaded onto a 60% sucrose pad and centrifuged to concentrate the samples, while the RG samples were resuspended from the pellet using 1 ml of normal or high $MgCl_2$ Granule buffer. For normal nuclease treatment groups, 1µl of RNAase I (100U/µ l;

catalog #AM2294, Thermo Fisher Scientific) was administered to the RC and RG and rotated at 4ºC for 30min. Then, 4ul of SuperaseIN (20U/µl; catalog # AM2969, Invitrogen) was added to the solution to halt the reaction. The samples are then loaded onto 15% to 60% sucrose gradient and centrifuged at 56,660 x g for 45 minutes to retrieve the monosomes from fraction 2 and 3. For high nuclease treatment group, RNAse I (10 U/ul, catalog #N6901K, Epicentre) was adjusted to the concentration of RC and RG via the A260 read from the Nanodrop. The OD obtained from the A260 read equals 6 unit. In other words, the amount of nuclease (µl) added equals A260 * 6 (U)/ 10 (µl/U). In addition, the samples are incubated at room temperature for 30 min instead of 4 ºC. Then, 6ul of SuperaseIN were added to halt the reaction. The samples were then spin at 68,000 xg for 3hrs on a Beckman tabletop ultracentrifuge to concentrate the monosomes, which pellets. The RNA of RC and RG was extracted through the trizole chloroform method followed by isopropanol precipitation to concentrate the samples. The samples were loaded onto Urea gel (catalog # EC68852Box, #EC68752Box, #EC62152Box, ThermoFisher) to select for RPF size. Segments between 25b and just above 40b were excised and retrieved to account for the possible longer fragments of the RPFs. The excised gels were frozen for 30 minutes on ice and then thawed overnight at room temperature. The RNA was extracted again with trizole chloroform extraction.

Linker Ligation:

The protocols follows improvements in RPF ligation (McGlincy and Ingolia, 2017). The concentration from the RNA footprint was calculated from Bioanalyzer small RNA kid (catalog # 5067-1548, Agilent). An equal amount of RNA was calculated and transferred to a new tube

for each sample to ensure each sample has a relatively equal amount after pooling. 3 different linkers (NI-810, NI-811, BI-812) were attached to each of the replicates. The samples were first dephosphorylated with T4PNK linker (catalog # M0351L, NEB), and then pre-adenylated linkers are attached through T4 Rnl2 (catalog # M0351L, NEB). The linked RNA was purified through excision of urea gel between 50bp and 70bp. Samples in the same variables were then pooled together with their gel fragment combined. The RNA was extracted from the gel with the steps stated previously containing all three replicates, followed by Reverse transcription. MyOne Streptavidin C1 DynaBeads (catalog#65001, ThermoFisher) was used for rRNA depletion. Lastly, PCR was performed. The samples were sequenced through the McGill University Genome Center on NovaSeq S1/2 flow cells.

RPF and RNA-SEQ data analysis

The raw reads were processed using Cutadapt (version 2.10), where sequences were trimmed to remove adapters and low-quality bases. Subsequently, demultiplexed each pooled reads runs using UMI barcodes (ID1=ATCGT, ID2=AGCTA and ID3=CGTAA). Additionally, options were used to trim N bases (--trim-n), discard sequences shorter than 18 bases (--minimum-length=18), allow a minimum overlap of 5 bases (--overlap=5), and omit insertions or deletions (--no-indels). Untrimmed reads were discarded, and logs of the trimming process were saved for quality control. Reads mapping to non-coding RNAs (ncRNAs) and ribosomal RNAs (rRNAs) were filtered out using Bowtie2 (version 2.3.5), aligning the reads against rRNA and ncRNA sequences from the Mus musculus reference (GRCm38, Ensembl release 102). The Bowtie2 parameters were set to maximize sensitivity (--very-sensitive). Unmapped reads were further

aligned to the Mus musculus genome (GRCm38, Ensembl release 102) using the STAR aligner (version 2.7.8a). The output was generated as transcript coordinate-sorted BAM files (--outSAMtype BAM SortedByCoordinate --quantMode TranscriptomeSAM). For some analyses PCR duplicates were identified and marked using *Picard MarkDuplicates* (version *2.26.6)*. These duplicates were then removed using *samtools* (version 1.19.2). Further, raw counts were obtained using featurecounts (version 2.2.0).

For RPKM and all DEG analysis, non-protein coding genes were removed. RPKM, reads per kilobase per million mapped reads, were calculated for abundances, which normalized the raw counts against gene length and total count. Occupancy for individual groups were calculated through performing DEG Analysis between RG raw count replicates and whole brain RNA seq replicates, and enrichment for individual groups were calculated through performing DEG Analysis between raw count RG replicates and raw count RC replicates. For comparison between WT and FMR1-KO groups, DEG Analysis was calculated as follow: abundances, raw count WT vs raw count FMR1-KO ; occupancy, raw count WT RG divided by whole brain RNA seq vs raw count FMR1-KO RG divided by whole brain RNA seq; enrichment, raw count WT RG divided by raw count WT RC vs raw count FMR1-KO RG divided by FMR1-KO RC.

The Differential Expression Gene Analysis was performed via R studio packages in *edgeR* from Bioconductor adapted for RNA-seq (Wu et al., 2021). Data were normalized for library size differences and filtered to remove lowly expressed genes. Results were ranked and evaluated based on adjusted p-value (FDR), which was calculated through the Benhamini-Hochberg method. GO Enrichment Analysis was performed with clusterprofiler (Wu et al.,

2021) and org.Mm.eg.db from Biomanager using R studio (Yu, 2024). Comparison to data online was performed via jupyter notebook and graphed by *boxplot* in *matplotlib*. The significance of each dataset comparison was done through performing t-test between the overlapped gene in our data and non-overlapped genes through the *statistics* function from python. The p-value was Bonferroni corrected.

We used transcript coordinate Bam files for peak analysis. Regions of the mRNA that have an abundant amount of RPFs were referred to as peaks (Anadolu et al., 2023). The peaks previously were selected through marking the inflection point within the abundances of RPFs. Here, we identify the highest point (zenith) in the peak after mapping RPFs to transcripts. To be identified as a peak, the zenith of an abundance site for the reads must be 4x higher of the average of the total transcript. Moreover, this zenith must be detected in all the biological samples (zenith within 6 nucleotides for each replicate). We first determine total peaks in all six samples (WT and FMR1-KO) and then determined peaks that were in all WT samples, but not in FMR1-KO samples (WT peaks; peaks lost in the absence of FMRP) and peaks that were present only in the FMR1-KO samples, but not in any WT samples (FMRP peaks).

For identification of motifs in the peaks, the zenith was extended on both sides by 17nt. Motif occurrences in the peaks were identified using FIMO from the MEME suite (Bailey et al., 2015) and universalmotif (Tremblay, 2024). Percentage peaks with FXS related motifs were identifying only the positive strand and limiting the score, or log-likelihood ratio, to 5, and normalizing against the total peaks. Biopython was utilized to convert peak sequences to amino acids.

Cryo-electron microscopy.

The purified fractions were treated with nuclease as described (Anadolu et al., 2023) before they were applied to the electron microscopy grids. The samples were applied to the grid in buffer containing 20mM Tris-HCl, ph 7.4; 150 mM NaCl; 10 mM $MgCl^{2+}$, and they were applied at a concentration of 180 nM. Cryo-EM grids (c-flat CF-2/2-2C-T) used for these samples were washed in chloroform for two hours and treated with glow discharged in air at 15 mA for 20 seconds. A volume of 3.6 µL was applied to the grid before vitrification in liquid ethane using a Vitrobot Mark IV (Thermo Fisher Scientific Inc.). The Vitrobot parameters used for vitrification were blotting time 3 seconds and a blot force +1. The Vitrobot chamber was set to 25 °C and 100% relative humidity.

All datasets were collected at FEMR-McGill using a Titan Krios microscope operated at 300 kV and equipped with a Gatan BioQuantum LS K3 direct electron detector. The software used for data collection was SerialEM (Schorb et al., 2019). Images were collected in counting mode at a nominal magnification of 81,000x, producing images with a calibrated pixel size of 1.09 Å. Movies for all datasets were collected using 30 frames with a total dose of 40 $e^-/Å^2$.

Image processing.

All the image processing steps were done using cryoSPARC v4.5 software (Punjani et al., 2017). A total of 10,866 cryo-EM movies were corrected for beam-induced motion correction using Patch Motion Correction using default settings that included using information up to 5Å resolution when aligning frames, a B-factor of 500 and a 0.5 calibrated smoothing constant applied to the trajectories. CTF parameter estimation was done using Patch CTF estimation

using default settings. The minimum and maximum resolution considered to estimate the CTF parameters were 25 Å and 4 Å, and the minimum and maximum defocus values were set up at 1,000 and 50,000 Å. The corrected micrographs were then curated by Manually Curate Exposures. For the particle-picking step, the Blob Picker program was first applied to 2,000 obtained micrographs using a circular blob with a minimum and maximum particle diameter of 200 Å and 480 Å. The maximum resolution considered during picking was 20 Å. The angular sampling used was 5 degrees, and the minimum particle separation distance was 0.5 (in units of particle diameters). The picked particles were extracted with a box size of 448 pixels, which was reduced to 112 pixels, and then subjected to 2D classification to generate the 2D templates for subsequent Template Picker using the 2,000 micrographs. In the 2D Classification step, we requested 50 classes and we selected 0.85 and 0.99 as inner and outer window radius. The maximum resolution considered in the images was 9 Å, and we used 2 for the initial uncertainty factor. The rest of the settings were used with the default parameters. The particles obtained from the Template Picker were curated again by 2D classification to remove the bad particles using the same job parameters. The curated particles were selected and used to train a model using Topaz (Bepler et al., 2019) with default settings, including a minibatch size of 128 and an expected number of particles of 165 per micrograph. The trained model was then used to pick particles from all the micrographs. The picked particles were subjected to 2 cycles of 2D Classification to remove junk particles. The obtained particles were then subjected to the subsequent particle curation step, which combined Ab-initio Reconstruction and Heterogeneous Refinement programs using default settings. For the Ab-Initio step, we selected 0.85 and 0.99 as inner and outer window radius, requested 3 classes and a maximum and minimum resolution to

consider of 35 Å and 12 Å. All other parameters for this routine were used with the default settings and values. The three initial Ab-initio models generated were subsequently used in a Heterogeneous Refinement using default parameters to separate the particles into multiple classes. The particles assigned to the class with unidentifiable features were discarded, whereas the particles assigned to reconstructions with ribosomal features were merged for subsequent processing. The total number of good particles after particle curation was 890,644.

To explore the structural heterogeneity, the curated set of particles was used to generate a consensus map using Non-Uniform Refinement with default settings and C1 symmetry. The aligned particles were then subjected to 3D Variability Analysis requesting 3 orthogonal principal modes and the subsequent 3D Variability Display 3D job was ru in cluster mode with all settings at default values. The number of clusters requested varied between experiments and ranged from 3 to 5. Results were filtered at 9 Å. Overall, we performed two rounds of the 3D Variability Analysis combined with 3D Variability Display to resolve the sample heterogeneity. Resulting maps from the exhaustive 3D classification were visually inspected in (Pettersen et al., 2004; Pettersen et al., 2021) and groups of particles representing similar structural features were merged. To obtain high-resolution structures, the particles from each class were extracted with a box size of 448 pixels and refined with Non-Uniform Refinement. The refinement jobs were run run under default settings with C1 symmetry, optimized per-particle defocus, optimized per-exposure group CTF parameters and options 'Fit Spherical Aberration', 'Fit tetrafoil' and 'Fit anisotropic Magnification' activated. To improve local resolution, Local Refinement was performed under default settings to refine the two subunits (40S and 60S) independently for all

the classes. Particle Subtraction run under default settings was used before Local Refinement to subtract the signal from the particle stacks that will not be used for Local refinement. Average resolution estimation and local resolution analysis were done with cryoSPARC using the gold-standard approach (Henderson et al., 2012). Cryo-EM map visualization was performed in UCSF Chimera and Chimera X (Pettersen et al., 2004; Pettersen et al., 2021)

Ribopuromycylation Assay

WT mouse and FMR1-KO mouse hippocampal neurons were dissected from P0 mouse and cultured on to poly-L-lysine (PLL)-coated 18mm coverslips as previously described (Langille et al., 2019). The hippocampal neurons were incubated with neurobasal media supplemented with 1% (vol/vol) N2 and penicillion/streptomycin, 2%(vol/vol) B27 and 0.5 mM GlutaMAX (Life Technologies). Treatment groups: +puro (puromycin), + anisomycin, +puro +HHT (homoharringtonine), and +puro + HHT + DHPG (S)-3,5-Dihydroxyphenylglycine) were assigned to cells and added to the culture on day 8. Cells that were assigned to HHT or HHT + DHPG conditions were preincubated with supplemented neural basal media as stated above with 5µM HHT (catalog # 1416, Tocris Bioscience) or with 5µM HHT and 100µM DHPG (catalog # 0805, Tocris Bioscience) for 15min in 37°C to ensure sufficient time for ribosomes to runoff and for DHPG to reactivate stalled ribosomes. The control +puro groups were incubated with supplemented neural basal media. The solution was then removed from all groups and replaced with new supplemented neural basal medium for the control group and supplemented neural basal medium with 100µM Puromycin (catalog# P7255, Sigma Aldric) for all the variable

groups. All groups were incubated at 37°C for 5min similar to previous experiments (Graber et al, 2013; Langille et al 2019). The cultures were then placed on ice and washed with HBS supplemented with 0.0003% digitonin for 2min, followed by 3x wash with HBS. The cultures were then placed at room temperature and fixed with 4% paraformaldehyde for 30 min. Upon completion, the cell cultures were washed with PBS three times, sealed in the 1x PBS, and placed at 4°C till immunocytochemistry.

Immunocytochemistry

Cultures were treated with 0.1% Triton-X 100 with 30% sucrose in PBS for 10min to allow for permeabilization of cell membrane followed by 15min of quench solution (55mM ammonium chloride in 1x PBS). The cultures were then washed in 1xPBX for three times before blocking with 1% BSA in PBS for 30min. The cultures were then incubated with primary antibody solution (1:1000 mouse anti-puromycin (DSHB Hybridoma Product PMY-2A4)) in 1% BSA and 1xPBS for 1hr. The primary antibody solution was then removed, and the cultures were then washed 3 times with 1xPBS. Secondary antibody solution (anti-mouse 1:1000 Alexa Fluor 745) were then added to the cultures and incubated for 1hr. The secondary antibody solutions were then removed, and the cultures were washed 3 times with 1xPBS. The culture contained coverslips were then removed and mounted using 10µL Dako mounting medium. The coverslips were stored in the dark before imaging.

Confocal Microscopy

Cells were imaged using a Zeiss LSM-900 confocal microscopy with a 63x oil immersion objective. The images were then assigned numbers and randomized to lower potential biases. ImageJ was used to straighten the neurites.

Quantification of RPM

Only cells with straightened neurites over 75 m were used. The person doing the quantification was blind to the treatment or genotype. The images were converted to 8 bits and then thresholded with a minimum of 180/256 pixel intensity although there was a manual component to this quantification based on the relative brightness of the image. The analyze particle Macro of Image J was used to identify puncta with size criteria of 0.15 to 2 μm^2 and circularity of 0.4-1.0. Only puncta>50 µm from the soma were considered for this analysis.

Data Availability.

The cryo-EM maps obtained in this study have been deposited in the Electron Microscopy Data Bank (EMDB), and the accession codes are detailed in Table S4-1. All sequences are available in the GEO database.

References

Anadolu MN, Sossin WS (2020) Focusing on mRNA granules and stalled polysomes amidst diverse mechanisms underlying mRNA transport, mRNA storage and local translation. In: Oxford Handbook of Neuronal Protein Synthesis (Sossin W, ed). Oxford Press.

Anadolu MN, Sun J, Li JT, Graber TE, Ortega J, Sossin WS (2024) Puromycin reveals a distinct conformation of neuronal ribosomes. Proc Natl Acad Sci U S A 121:e2306993121.

Anadolu MN, Sun J, Kailasam S, Chalkiadaki K, Krimbacher K, Li JT, Markova T, Jafarnejad SM, Lefebvre F, Ortega J, Gkogkas CG, Sossin WS (2023) Ribosomes in RNA Granules Are Stalled on mRNA Sequences That Are Consensus Sites for FMRP Association. J Neurosci 43:2440-2459.

Anderson BR, Chopra P, Suhl JA, Warren ST, Bassell GJ (2016) Identification of consensus binding sites clarifies FMRP binding determinants. Nucleic Acids Res 44:6649-6659.

Ascano M, Jr., Mukherjee N, Bandaru P, Miller JB, Nusbaum JD, Corcoran DL, Langlois C, Munschauer M, Dewell S, Hafner M, Williams Z, Ohler U, Tuschl T (2012) FMRP targets distinct mRNA sequence elements to regulate protein expression. Nature 492:382-386.

Aschrafi A, Cunningham BA, Edelman GM, Vanderklish PW (2005) The fragile X mental retardation protein and group I metabotropic glutamate receptors regulate levels of mRNA granules in brain. Proc Natl Acad Sci U S A 102:2180-2185.

Bagni C, Zukin RS (2019) A Synaptic Perspective of Fragile X Syndrome and Autism Spectrum Disorders. Neuron 101:1070-1088.

Bailey TL, Johnson J, Grant CE, Noble WS (2015) The MEME Suite. Nucleic Acids Res 43:W39-49.

Batish M, van den Bogaard P, Kramer FR, Tyagi S (2012) Neuronal mRNAs travel singly into dendrites. Proc Natl Acad Sci U S A 109:4645-4650.

Bepler T, Morin A, Rapp M, Brasch J, Shapiro L, Noble AJ, Berger B (2019) Positive-unlabeled convolutional neural networks for particle picking in cryo-electron micrographs. Nat Methods 16:1153-1160.

Darnell JC, Mostovetsky O, Darnell RB (2005) FMRP RNA targets: identification and validation. Genes Brain Behav 4:341-349.

Darnell JC, Van Driesche SJ, Zhang C, Hung KY, Mele A, Fraser CE, Stone EF, Chen C, Fak JJ, Chi SW, Licatalosi DD, Richter JD, Darnell RB (2011) FMRP stalls ribosomal translocation on mRNAs linked to synaptic function and autism. Cell 146:247-261.

David A, Bennink JR, Yewdell JW (2013) Emetine optimally facilitates nascent chain puromycylation and potentiates the ribopuromycylation method (RPM) applied to inert cells. Histochem Cell Biol 139:501-504.

Debanne D, Campanac E, Bialowas A, Carlier E, Alcaraz G (2011) Axon physiology. Physiol Rev 91:555-602.

Deng PY, Klyachko VA (2021) Channelopathies in fragile X syndrome. Nat Rev Neurosci 22:275-289.

Duchaine T, Wang HJ, Luo M, Steinberg SV, Nabi IR, DesGroseillers L (2000) A novel murine Staufen isoform modulates the RNA content of Staufen complexes. Mol Cell Biol 20:5592-5601.

El Fatimy R, Davidovic L, Tremblay S, Jaglin X, Dury A, Robert C, De Koninck P, Khandjian EW (2016) Tracking the Fragile X Mental Retardation Protein in a Highly Ordered Neuronal RiboNucleoParticles Population: A Link between Stalled Polyribosomes and RNA Granules. PLoS Genet 12:e1006192.

Elvira G, Wasiak S, Blandford V, Tong XK, Serrano A, Fan X, del Rayo Sanchez-Carbente M, Servant F, Bell AW, Boismenu D, Lacaille JC, McPherson PS, DesGroseillers L, Sossin WS (2006) Characterization of an RNA granule from developing brain. Molecular & cellular proteomics : MCP 5:635-651.

Enam SU, Zinshteyn B, Goldman DH, Cassani M, Livingston NM, Seydoux G, Green R (2020) Puromycin reactivity does not accurately localize translation at the subcellular level. Elife 9.

Fernandopulle MS, Lippincott-Schwartz J, Ward ME (2021) RNA transport and local translation in neurodevelopmental and neurodegenerative disease. Nat Neurosci 24:622-632.

Garreau de Loubresse N, Prokhorova I, Holtkamp W, Rodnina MV, Yusupova G, Yusupov M (2014) Structural basis for the inhibition of the eukaryotic ribosome. Nature 513:517-522.

Graber TE, Hebert-Seropian S, Khoutorsky A, David A, Yewdell JW, Lacaille JC, Sossin WS (2013) Reactivation of stalled polyribosomes in synaptic plasticity. Proc Natl Acad Sci U S A 110:16205-16210.

Graber TE, Freemantle E, Anadolu MN, Hebert-Seropian S, MacAdam RL, Shin U, Hoang HD, Alain T, Lacaille JC, Sossin WS (2017) UPF1 Governs Synaptic Plasticity through Association with a STAU2 RNA Granule. J Neurosci 37:9116-9131.

Hansen JL, Moore PB, Steitz TA (2003) Structures of five antibiotics bound at the peptidyl transferase center of the large ribosomal subunit. J Mol Biol 330:1061-1075.

Henderson R et al. (2012) Outcome of the first electron microscopy validation task force meeting. Structure 20:205-214.

Hobson BD, Kong L, Hartwick EW, Gonzalez RL, Sims PA (2020) Elongation inhibitors do not prevent the release of puromycylated nascent polypeptide chains from ribosomes. Elife 9.

Holt CE, Martin KC, Schuman EM (2019) Local translation in neurons: visualization and function. Nat Struct Mol Biol 26:557-566.

Hou L, Antion MD, Hu D, Spencer CM, Paylor R, Klann E (2006) Dynamic translational and proteasomal regulation of fragile X mental retardation protein controls mGluR-dependent long-term depression. Neuron 51:441-454.

Huber KM, Gallagher SM, Warren ST, Bear MF (2002) Altered synaptic plasticity in a mouse model of fragile X mental retardation. Proc Natl Acad Sci U S A 99:7746-7750.

Ingolia NT (2014) Ribosome profiling: new views of translation, from single codons to genome scale. Nat Rev Genet 15:205-213.

Ishizuka N, Cowan WM, Amaral DG (1995) A quantitative analysis of the dendritic organization of pyramidal cells in the rat hippocampus. J Comp Neurol 362:17-45.

Khayachi A, Gwizdek C, Poupon G, Alcor D, Chafai M, Casse F, Maurin T, Prieto M, Folci A, De Graeve F, Castagnola S, Gautier R, Schorova L, Loriol C, Pronot M, Besse F, Brau F, Deval E, Bardoni B, Martin S (2018) Sumoylation regulates FMRP-mediated dendritic spine elimination and maturation. Nat Commun 9:757.

Kiebler MA, Bassell GJ (2006) Neuronal RNA Granules: Movers and Makers. Neuron 51:685-690.

Kipper K, Mansour A, Pulk A (2022) Neuronal RNA granules are ribosome complexes stalled at the pre-translocation state. J Mol Biol 434:167801.

Krichevsky AM, Kosik KS (2001) Neuronal RNA granules: a link between RNA localization and stimulation-dependent translation. Neuron 32:683-696.

Kurosaki T, Mitsutomi S, Hewko A, Akimitsu N, Maquat LE (2022) Integrative omics indicate FMRP sequesters mRNA from translation and deadenylation in human neuronal cells. Mol Cell 82:4564-4581 e4511.

Langille JJ, Ginzberg K, Sossin WS (2019) Polysomes identified by live imaging of nascent peptides are stalled in hippocampal and cortical neurites. Learn Mem 26:351-362.

Maurin T, Lebrigand K, Castagnola S, Paquet A, Jarjat M, Popa A, Grossi M, Rage F, Bardoni B (2018) HITS-CLIP in various brain areas reveals new targets and new modalities of RNA binding by fragile X mental retardation protein. Nucleic Acids Res 46:6344-6355.

McGlincy NJ, Ingolia NT (2017) Transcriptome-wide measurement of translation by ribosome profiling. Methods 126:112-129.

Niere F, Wilkerson JR, Huber KM (2012) Evidence for a fragile X mental retardation protein-mediated translational switch in metabotropic glutamate receptor-triggered Arc translation and long-term depression. J Neurosci 32:5924-5936.

Nosyreva ED, Huber KM (2006) Metabotropic receptor-dependent long-term depression persists in the absence of protein synthesis in the mouse model of fragile X syndrome. J Neurophysiol 95:3291-3295.

Ntoulas G, Brakatselos C, Nakas G, Asprogerakas MZ, Delis F, Leontiadis LJ, Trompoukis G, Papatheodoropoulos C, Gkikas D, Valakos D, Vatsellas G, Politis PK, Polissidis A, Antoniou K (2024) Multi-level profiling of the Fmr1 KO rat unveils altered behavioral traits along with aberrant glutamatergic function. Transl Psychiatry 14:104.

Pettersen EF, Goddard TD, Huang CC, Couch GS, Greenblatt DM, Meng EC, Ferrin TE (2004) UCSF Chimera--a visualization system for exploratory research and analysis. J Comput Chem 25:1605-1612.

Pettersen EF, Goddard TD, Huang CC, Meng EC, Couch GS, Croll TI, Morris JH, Ferrin TE (2021) UCSF ChimeraX: Structure visualization for researchers, educators, and developers. Protein Sci 30:70-82.

Punjani A, Rubinstein JL, Fleet DJ, Brubaker MA (2017) cryoSPARC: algorithms for rapid unsupervised cryo-EM structure determination. Nat Methods 14:290-296.

Qin M, Kang J, Burlin TV, Jiang C, Smith CB (2005) Postadolescent changes in regional cerebral protein synthesis: an in vivo study in the FMR1 null mouse. J Neurosci 25:5087-5095.

Richter JD, Zhao X (2021) The molecular biology of FMRP: new insights into fragile X syndrome. Nat Rev Neurosci 22:209-222.

Richter JD, Bassell GJ, Klann E (2015) Dysregulation and restoration of translational homeostasis in fragile X syndrome. Nat Rev Neurosci 16:595-605.

Santini E, Klann E (2014) Reciprocal signaling between translational control pathways and synaptic proteins in autism spectrum disorders. Sci Signal 7:re10.

Sawicka K, Hale CR, Park CY, Fak JJ, Gresack JE, Van Driesche SJ, Kang JJ, Darnell JC, Darnell RB (2019) FMRP has a cell-type-specific role in CA1 pyramidal neurons to regulate autism-related transcripts and circadian memory. Elife 8.

Schorb M, Haberbosch I, Hagen WJH, Schwab Y, Mastronarde DN (2019) Software tools for automated transmission electron microscopy. Nat Methods 16:471-477.

Shah S, Molinaro G, Liu B, Wang R, Huber KM, Richter JD (2020) FMRP Control of Ribosome Translocation Promotes Chromatin Modifications and Alternative Splicing of Neuronal Genes Linked to Autism. Cell Rep 30:4459-4472 e4456.

Sossin WS, DesGroseillers L (2006) Intracellular trafficking of RNA in neurons. Traffic 7:1581-1589.

Thomson SR, Seo SS, Barnes SA, Louros SR, Muscas M, Dando O, Kirby C, Wyllie DJA, Hardingham GE, Kind PC, Osterweil EK (2017) Cell-Type-Specific Translation Profiling Reveals a Novel Strategy for Treating Fragile X Syndrome. Neuron 95:550-563 e555.

Tremblay BJ (2024) universalmotif: An R package for biological motif analysis. Journal of Open Source Software 9:7012.

Udagawa T, Farny NG, Jakovcevski M, Kaphzan H, Alarcon JM, Anilkumar S, Ivshina M, Hurt JA, Nagaoka K, Nalavadi VC, Lorenz LJ, Bassell GJ, Akbarian S, Chattarji S, Klann E, Richter JD (2013) Genetic and acute CPEB1 depletion ameliorate fragile X pathophysiology. Nat Med 19:1473-1477.

Wong HH, Watt AJ, Sjostrom PJ (2024) Synapse-specific burst coding sustained by local axonal translation. Neuron 112:264-276 e266.

Wu T, Hu E, Xu S, Chen M, Guo P, Dai Z, Feng T, Zhou L, Tang W, Zhan L, Fu X, Liu S, Bo X, Yu G (2021) clusterProfiler 4.0: A universal enrichment tool for interpreting omics data. Innovation (Camb) 2:100141.

Yoon BC, Zivraj KH, Holt CE (2009) Local translation and mRNA trafficking in axon pathfinding. Results Probl Cell Differ 48:269-288.

Yu G (2024) Thirteen years of clusterProfiler. Innovation (Camb) 5:100722.

Yu TW, Berry-Kravis E (2014) Autism and fragile X syndrome. Semin Neurol 34:258-265.

Zhang G, Xu Y, Wang X, Zhu Y, Wang L, Zhang W, Wang Y, Gao Y, Wu X, Cheng Y, Sun Q, Chen D (2022) Dynamic FMR1 granule phase switch instructed by m6A modification contributes to maternal RNA decay. Nat Commun 13:859.

FIGURE LEGENDS

Figure 1. Characterization of Sucrose Gradient Sedimentation.

A) A summary of protocol for isolating the RNA Granules (RG) from C57 and FMR1-KO mouse whole brain homogenate using sucrose gradient fractionation. B) SDS-page stained with Coomassie brilliant blue showing the distribution of proteins from each fraction of the sucrose gradient from WT mouse and rat brains. Equal volumes of resuspended ethanol precipitates (fractions 1-10) and resuspended pellet were used. C) Representative immunoblots for WT and FMR1-KO mouse starting materials (brain homogenate), ribosomal cluster (RC; fraction 5/6) and RNA Granules (RG; pellet). D-F) The Quantification of S6 (N = 6) was normalized to the level of S6 in the starter fraction. The quantification of UPF1 (N = 6), Stau2 59kD (N = 5) and Stau2 52kD (N = 5) from RC and RG was normalized to the level of S6 in that fraction, and then normalized again to the ratio of that protein and S6 in the starter fraction. H-K) The Quantification of enrichment of RG from RC (RG/RC) between FMR1-KO and WT samples for s6 (N = 6; $p = 0.008$), UPF1 (N = 6; $p>0.05$), Stau2 59kD (N = 5; $p>0.05$), and Stau2 52kD (N = 5;$p>0.05$). Error bars are Standard Error of the Mean; Student's T-test.

Figure 2. Loss of FMR1 does not affect anisomycin-purmycin competition.

A) A summary of protocol for anisomycin and puromycin competition on the RNA granule fraction. B) Top: Representative immunoblot stained with antibodies to puromycin (anti-puro) to showcase the inhibition of puromycylation (100 uM) by anisomycin (100 uM) in liver polyribosomes. Bottom: Corresponding membrane stained with ponceau before immunoblotting. The experiment was replicated twice with similar results. C) Top: Representative immunoblot that stained with anti-puromycin (anti-puro) to showcase the inhibition of puromycylation (100

uM) by anisomycin (100 uM) in Rat RG, WT mouse RG and FMR1-KO mouse RG. Bottom: Corresponding membrane stained with ponceau before immunoblotting. D) Quantification of percentage puromycylation resistant to anisomycin inhibition in Rat RG (N = 3), WT mouse RG (N = 4), FMR1-KO RG (N = 4). All groups are insignificant from each other (one way ANOVA, $p > 0.05$).

Figure 3. Higher Nuclease reduces size of RPFs in WT RNA granules.

A) A summary of protocol for ribosomal footprinting procedure. B) Representative image for size distribution of normalized footprint reads from high magnesium and high nuclease treatment group (M) and normal magnesium and normal nuclease treatment group (WT) for RPFs derived from the RNA granule fraction. C) Representative image for read coverage for M WT RNA Granule and WT RNA Granule UTR, untranslated region; CDS, coding sequence. D) Representative image for the number of read extremities (shading) for each read length (Y-axis) based on the distance from start(left) to stop(right) with the 5' end (top) and 3' end (bottom) for M WT RNA Granule and WT RNA Granule. E) Representative image for the periodicity statistics for each read coverage RPFs. Though the representative images above only included one replicate for the result, the data are shown in all replicates for both WT and FMR1-KO groups.

Figure 4. High Magnesium buffer does not affect ribosome structure, but leads to less sedimentation of secretory mRNAs.

(A) Composite cryo-EM maps of class 1 (A) and class 2 (B) 80S ribosomes found in the GF after purification in high magnesium buffer and RNase I treatment. The top panels show a side view of

the two classes of ribosome particles contained in the sample. The bottom panels show top views of the same cryo-EM maps. The 40S and 60S subunits are shown as transparent densities for easier viewing of the position of the tRNA molecules in each class. B) Gene Ontology (GO) terms of the significant genes from the differential expression gene (DEG) analysis of WT RG and WT M RG for 1) top: Biological Function 2) middle: Cellular Components and 3) bottom: Molecular

Figure 5: Assessment of RPF abundance, occupancy and enrichment in RGs of WT and FMRI-KO mice.

A) A summary of protocol to generate RPF abundance, occupancy and enrichment. B) GO terms of the WT M RG (left) and FMR1-KO (right)for abundance (top), occupancy (Middle) and enrichment (bottom). For each graph, GO terms from the top 500 genes: Biological Function (top), Cellular Components (middle), and Molecular Function (bottom).

Figure 6: Comparison of putative stalled mRNAs vs Total mRNAs in RPFs from the RG of WT and FMR1-KO mice.

Comparison of mRNAs associated to ribosome resistant of initiation inhibitor run-off (Shah et al., 2020) and FMRP-CLIPped mRNAs (Maurin et al., 2018; Darnel et al., 2011) to all other mRNAs. A) WT Granule abundance, B) FMR1-KO Granule M abundance, C) WT Granule Occupancy, D) FMR1-KO Granule Occupancy, E) WT Granule Enrichment, and F) FMR1-KO Granule Enrichment. P-values from each set were calculated by performing student t-test between the mRNAs that matched to the published dataset and the ones that did not.

Figure 7. Comparison of putative stalled mRNAs between WT and FMR1-KO mice.

Fold change between A) WT and FMR1 fold change in RG abundance (Shah average = 0.047; Maurin average = 0.086; Darnell average = 0.079), B) WT and FMR1 fold change in RG occupancy, C) WT and FMR1 fold change in RG enrichment, and D) WT and FMR1 fold change in RC abundance in comparison to mRNAs associated to ribosome resistant of initiation inhibitor run-off (Shah et al., 2020), FMRP-CLIPped mRNAs (Maurin et al., 2018; Darnel et al., 2011). P-values from each trait were calculated by performing student t-test between the mRNAs that matched to the published dataset and the ones that did not.

Figure 8: Comparison of RPF peaks in the RG of WT and FMR1-KO mice.

A) Representation of how peaks of RPFs are selected. B) Table of the number of peaks between replicates of WT RNA Granule (N = 3), FMR1-KO RNA Granule (N = 3) and combined (N = 6), and the percentage of peaks with FXS related motif. C) Example of RPF producing consensus peaks over the entire length of Tubb2b. Asterisks indicate consensus peaks (seen in all six samples with peaks within 6 bp).

Figure 9. RPM of hippocampal cultures derived from WT and FMR1-KO mice.

A) Summary of the protocol for puromycylation HHT-Runoff and DHPG Reactivation on WT and FMR1-KO hippocampal culture. B) Representative confocal images for puromycylated ribosomes with or without HHT runoff and DHPG reactivation. Circle denotes puromycin puncta. No visible staining was seen in the absence of puromycin. Scale bar shown below C) Quantification of RPM puncta density of puncta>50 microns from the cell body. Numbers are neurites/cultures. WT (42/5); WT DHPG (54/5), FMR1-KO (41/4), FMR1-KO DHPG (25/3). One way ANOVA ($F_{158,3}$= 5.32, $p< 0.005$) *, $p<0.05$ post-Hoc Tukey HSD test. D)

Quantification of size of RPM puncta >50 microns from the cell body. WT 189/5; WTDHPG 5171/5, FMR1 KO (118/4), FMRP KO DHPG (48/3). One way ANOVA showed no significance (P>0.5).

Supplemental Figures

Figure S3-1. Higher Nuclease reduces size of RPFs in FMR1-KO RGs .

A) A summary of protocol for ribosomal footprinting procedure. B) Representative image for size distribution of normalized footprint reads from high magnesium and high nuclease treatment group (M FMRI-KO RNA Granule) and normal magnesium and normal nuclease treatment group (FMR1-KO RNA Granule). C) Representative image for read coverage for M FMR1-KO RNA Granule and FMR1-KO RNA Granule. D) Representative image for the number of read extremities (shading) for each read length (Y-axis) based on the distance from start(left) to stop(right) with the 5' end (top) and 3' end (bottom) for M FMR1-KO RNA Granule and FMRI-KO RNA Granule. E) Representative image for the periodicity statistics for each read coverage RPFs.

Figure S3-2. Higher Nuclease reduces size of RPFs in FMR1-KO RCs .

A) A summary of protocol for ribosomal footprinting procedure. B) Representative image for size distribution of normalized footprint reads from high magnesium and high nuclease treatment group (M FMRI-KO RC) and normal magnesium and normal nuclease treatment group (FMR1-KO RC). C) Representative image for read coverage for M FMR1-KO RC and FMR1-KO RC. D) Representative image for the number of read extremities (shading) for each read length (Y-axis) based on the distance from start(left) to stop(right) with the 5' end (top) and 3' end

(bottom) for M FMR1-KO RC and FMRI-KO RC. E) Representative image for the periodicity statistics for each read coverage RPFs.

Figure S3-3. Higher Nuclease reduces size of RPFs in WT RCs .

A) A summary of protocol for ribosomal footprinting procedure. B) Representative image for size distribution of normalized footprint reads from high magnesium and high nuclease treatment group (M FMRI-KO RC) and normal magnesium and normal nuclease treatment group (WT RC). C) Representative image for read coverage for M WT RC and WT RC. D) Representative image for the number of read extremities (shading) for each read length (Y-axis) based on the distance from start(left) to stop(right) with the 5' end (top) and 3' end (bottom) for M WT RC and FMRI-KO RC. E) Representative image for the periodicity statistics for each read coverage RPFs.

Supplementary Figure S4-1. Single particle analysis image processing workflow. The cryo-EM dataset obtained for the GF after purification in high magnesium buffer and RNase I treatment was subjected to the image processing workflow in the figure. The diagram displays the main image processing steps undertaken with this dataset and the two main ribosome populations that were found as a result of the image classification approaches. The resolutions for the consensus maps and each one of the subunits in the maps obtained through local refinement are also indicated.

Supplementary Figure S4-2. Resolution analysis of the two major classes of 80S ribosomes in the Granule Fraction purified under high magnesium conditions.

Consensus cryo-EM maps (left panels) were initially calculated for class 1 (A) and class 2 (B) from the RNase I-treated Granule Fraction purified under high magnesium buffer conditions. These maps were subsequently refined by local refinement by dividing the 80S ribosome into two major bodies, the 60S and the 40S particles. The top panels in (A) and (B) show the local resolution analysis of the 80S consensus and composite maps obtained using local refinement. Composite maps were obtained by aligning them and merging the 60S and 40S cryo-EM maps obtained by local refinement using the command 'vop add' in Chimera. Maps are colored according to their local resolution using the color coding indicated in the scale bars. The Fourier shell correlation (FSC) curves for the consensus maps and each one of the subunits after the maps were subjected to local refinement are shown for class 1 and 2. For each class, we show the following FSC plots: 'No mask': the raw FSC calculated between two independent half-maps reconstructed from the data and no masking applied. 'Loose': FSC calculated after applying a loose soft solvent mask to both half maps. The loose mask is calculated by thresholding the density map at 50% of the maximum density value. The resulting volume is dilated to create a soft mask. Voxels in the mask within 25 angstroms of the thresholded region receive a mask value of 1.0. Voxels between 25 and 40 angstroms fall off with a soft cosine edge, and voxels outside 40 angstroms receive a value of 0.0. 'Tight': FSC calculated after applying a tight soft solvent mask to both half maps. The tight mask is calculated by the same procedure as the loose mask, except that the dilation distances are 6 angstroms for the value 1.0 distance and 12 angstroms for the value 0.0 distance. 'Corrected': FSC curve calculated using the tight mask with correction by noise substitution as described in Chen et al. (PMID: 23872039). In brief, the two half maps have their phases randomized beyond a certain resolution, then the tight mask is applied to both, and an FSC is calculated. This FSC is used along with the original FSC before phase randomization to compute the corrected FSC. This

accounts for correlation effects induced by masking. The resolution at which phase randomization begins is the resolution at which the no-mask FSC drops below the FSC = 0.143 criterion. We used a FSC threshold of 0.143 to report the overall resolution of the maps. The 'Viewing direction distribution' plot in panels (A) and (B) show the orientation distribution of the particles contributing to the cryo-EM map for each one of the classes. These plots are 2D histograms that show the number of particles with a viewing direction at a particular elevation/azimuth bin. The number of particles can be inferred by the color code scale bar to the right of each plot.
y the color code scale bar to the right of each plot.

Supplementary Figure S8-1. Comparison of RPF peaks in the RG of WT and FMR1-KO mice with PCR duplication removed.

A) A summary for peak selection process to remove PCR duplicates based on the randomized UMI. B) PCR duplication percentage in WT RPF (N= 3) and FMR1-KO RPF replicates (N=3). C) Example of RPF producing consensus peaks over the entire length of Tubb2b generated from samples without PCR duplicates removed and samples with PCR duplicates removed. D) Table of the number of peaks, the percentage of peaks with FXS related motif, and the negative charged amino acid Asp (aspartic acid) and Glu (Glutamic Acid) generated from WT RG (N = 3), FMR1-KO RG (N = 3) and combined (N = 6) with PCR duplicates removed.

Supplementary Figure S9-1. Effect of Anisomycin and HHT on RPM of hippocampal cultures derived from WT and FMR1-KO mice.

A) Representative confocal images for puromycylated ribosomes treated either with puromycin and anisomycin together or pre-treated with HHT for 15 minutes before treating with puromycin. Circle denotes puromycin puncta. No visible staining was seen in the absence of puromycin. Quantification of RPM puncta density of puncta>50 microns from the cell body compared to WT (see Fig. 9). There is no effect of adding anisomycin with puromycin or preincubation with HHT on the puncta density (B,D) or puncta size (C, E) in WT (B,C) or FMRP (D,E). WT numbers are the same as Figure 9. Numbers are neurites/cultures. Puncta Density WT (42/5); WT anisomycin (A) (27/4); WT homoharringtonin (H) (36/5), FMR1-KO (41/4), FMR1-KO anisomycin (A) (23/3), FMRP homoharringtonin (45,5). One way ANOVA showed no significance for density or size (P>0.5).

Supplementary Tables

Supplementary Table 4-1. Data acquisition, reconstruction and refinement parameters and data deposition codes for the cryo-EM dataset.

	80S Class 1 (A/P & P/E tRNA*)	80S Class 2 (P/P tRNA*)
Data Collection		
Microscope	Titan Krios	
Detector	Gatan BioQuantum LS K3	
Nominal Magnification	81,000x	
Voltage (kV)	300	
Total exposure ($e^-/Å^2$)	40	
Number of frames	30	
Defocus range (μm)	-1.25 to -2.75	
Calibrated physical pixel size (Å/px)	1.09	
Reconstruction and Refinement		
Particle number	698,894	141,803
Resolution (Å)	Consensus map (CM): 80S (2.7Å) Multi-body refinement (MBR): 40S (3.3Å) & 60S (2.7 Å)	CM: 80S (3.2Å) MBR: 40S (4.5Å) & 60S (3.2 Å)

Data Deposition		
EMDB code	EMDB-XXXXX	EMDB-YYYYY

* A/P tRNA: Aminoacyl / Peptidyl transfer RNA; P/P tRNA: Peptidyl / Peptidyl transfer RNA.

Supplemental Extended Data Tables

Extended Data Table S3-1.List of Genes with high ratios of long reads/short reads in M WT samples

Extended Data Table S4-1. DEG and GO analysis comparing samples with high nuclease high Magnesium (M) and normal treatment (N).

Extended Data Table S5-1. RNA Seq and RKPM for all M samples for all genes. Occupancy and Enrichment calculations for WT and FMR1-KO M samples.

Extended Data Table S5-2. DEG analyses comparing WT and FMR-1 KO

Extended Data Table S5-3 GO analysis of WT and FMR1-KO

Extended Data Table S6-1 Abundance, Occupancy and Enrichment for WT and FMR1-KO M samples matching the Shah, Maurin and Darnell Lists.

Extended Data Table S8-1. List of all Peaks from M samples present in all six samples (Total) or just FMR1-KO samples or just WT samples as well as Motif counts for all these samples.

Extended Data Table S8-2 Amino acid enrichment of Peaks

Extended Data Table S8-3. Using data with no PCR duplicates. List of all Peaks from M samples present in all six samples (Total) or just FMR1-KO samples or just WT samples as well as Motif counts for all these samples.

Figure 1

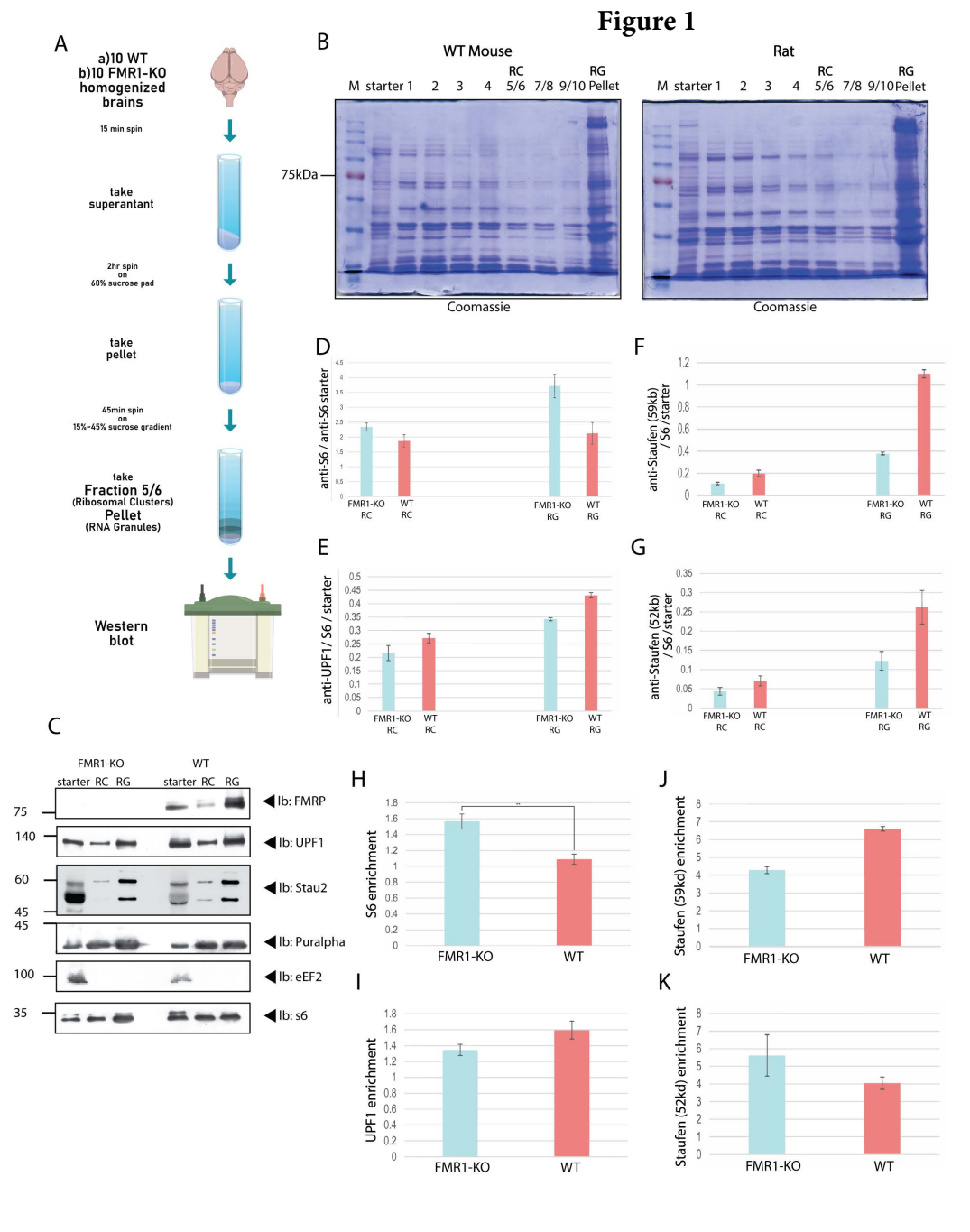
A
a)10 WT
b)10 FMR1-KO
homogenized
brains
15 min spin
take
superantant
2hr spin
on
60% sucrose pad
take
pellet
45min spin
on
15%-45% sucrose gradient
take
Fraction 5/6
(Ribosomal Clusters)
Pellet
(RNA Granules)
Western
blot
B
WT Mouse
Rat
M starter 1 2 3 4 RC 5/6 7/8 9/10 RG Pellet
75kDa
Coomassie
C
FMR1-KO
WT
starter RC RG
Ib: FMRP
Ib: UPF1
Ib: Stau2
Ib: Puralpha
Ib: eEF2
Ib: s6
D
anti-S6 / anti-S6 starter
E
anti-UPF1/ S6 / starter
F
anti-Staufen (59kb) / S6 /starter
G
anti-Staufen (52kb) / S6 /starter
FMR1-KO RC
WT RC
FMR1-KO RG
WT RG
H
S6 enrichment
I
UPF1 enrichment
J
Staufen (59kd) enrichment
K
Staufen (52kd) enrichment
FMR1-KO
WT

Figure 2

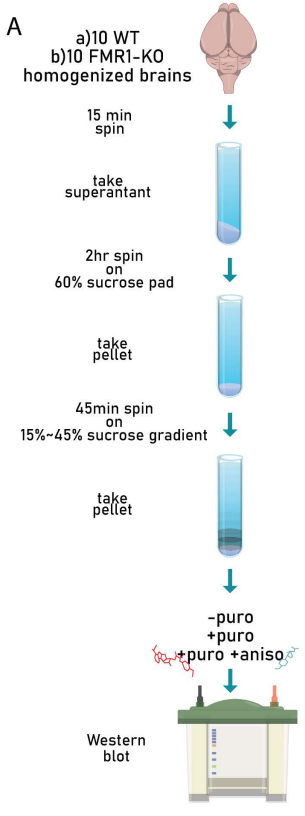
A
a)10 WT
b)10 FMR1-KO
homogenized brains
15 min
spin
take
superantant
2hr spin
on
60% sucrose pad
take
pellet
45min spin
on
15%~45% sucrose gradient
take
pellet
-puro
+puro
+puro +aniso
Western
blot

B
Liver
-puro +puro +puro
+aniso
anti-puro
Ponceau

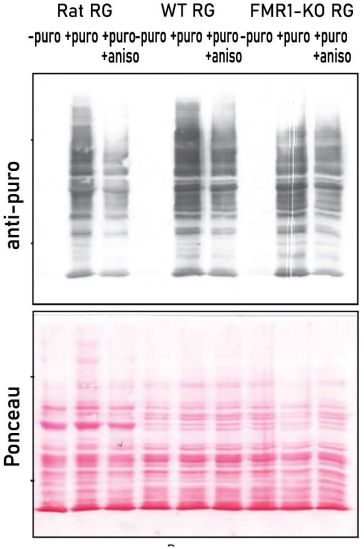
C
Rat RG
WT RG
FMR1-KO RG
-puro +puro +puro
+aniso
-puro +puro +puro
+aniso
-puro +puro +puro
+aniso
anti-puro
Ponceau

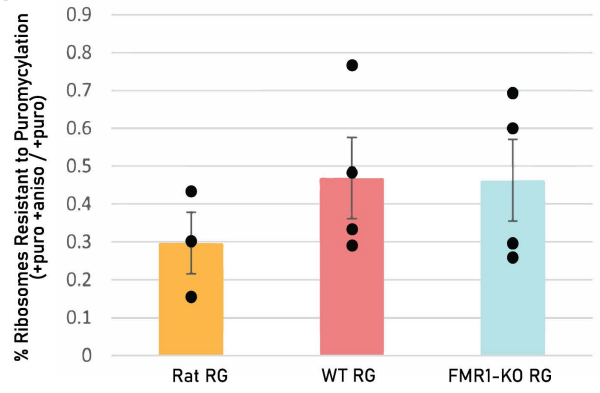
D
% Ribosomes Resistant to Puromycylation
(+puro +aniso / +puro)
0.9
0.8
0.7
0.6
0.5
0.4
0.3
0.2
0.1
0
Rat RG
WT RG
FMR1-KO RG

Figure 3

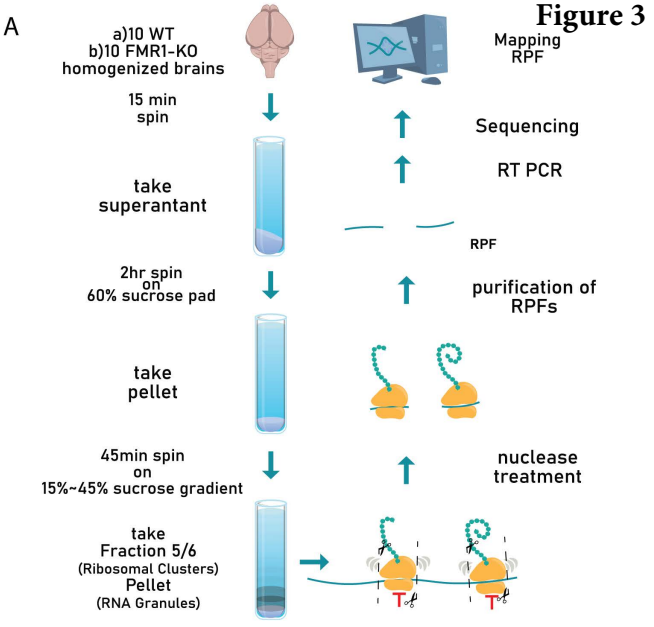
A
a)10 WT
b)10 FMR1-KO
homogenized brains
15 min
spin
take
superantant
2hr spin
on
60% sucrose pad
take
pellet
45min spin
on
15%~45% sucrose gradient
take
Fraction 5/6
(Ribosomal Clusters)
Pellet
(RNA Granules)
Mapping
RPF
Sequencing
RT PCR
RPF
purification of
RPFs
nuclease
treatment

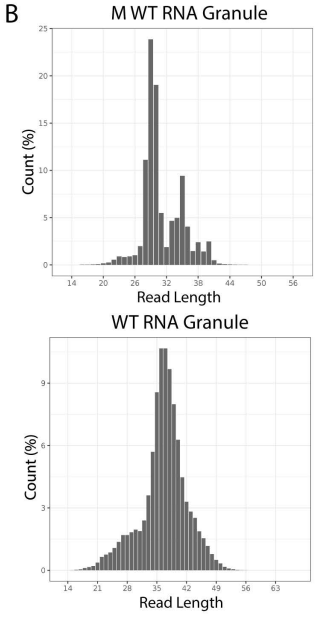
B
M WT RNA Granule
Count (%)
Read Length
WT RNA Granule
Count (%)
Read Length

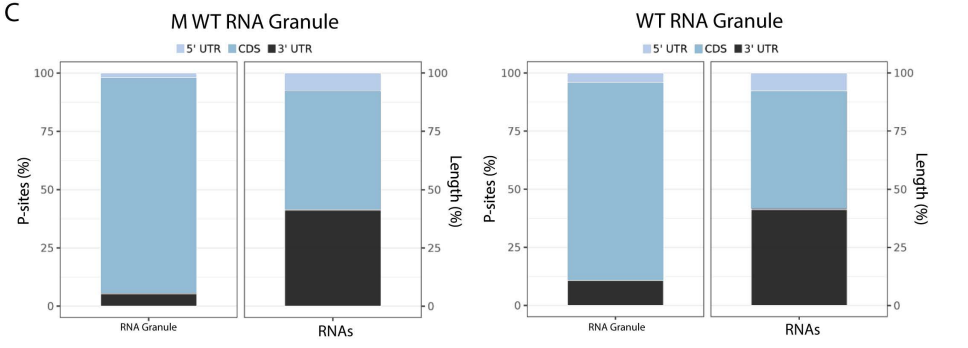
C
M WT RNA Granule
5' UTR
CDS
3' UTR
P-sites (%)
Length (%)
RNA Granule
RNAs
WT RNA Granule
5' UTR
CDS
3' UTR
P-sites (%)
Length (%)
RNA Granule
RNAs

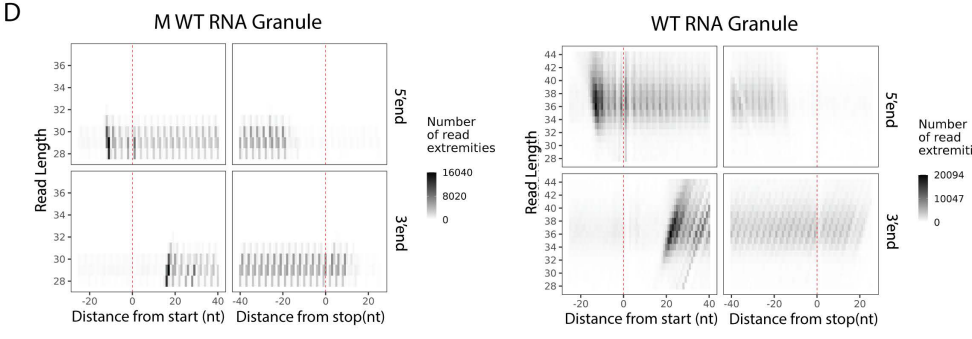
D
M WT RNA Granule
Read Length
5'end
3'end
Number
of read
extremities
16040
8020
0
Distance from start (nt)
Distance from stop(nt)
WT RNA Granule
Read Length
5'end
3'end
Number
of read
extremities
20094
10047
0
Distance from start (nt)
Distance from stop(nt)

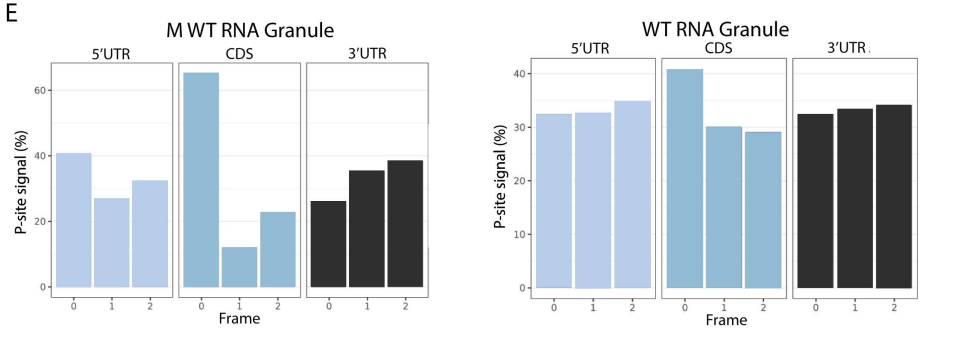
E
M WT RNA Granule
5'UTR
CDS
3'UTR
P-site signal (%)
Frame
WT RNA Granule
5'UTR
CDS
3'UTR
P-site signal (%)
Frame

Figure 4

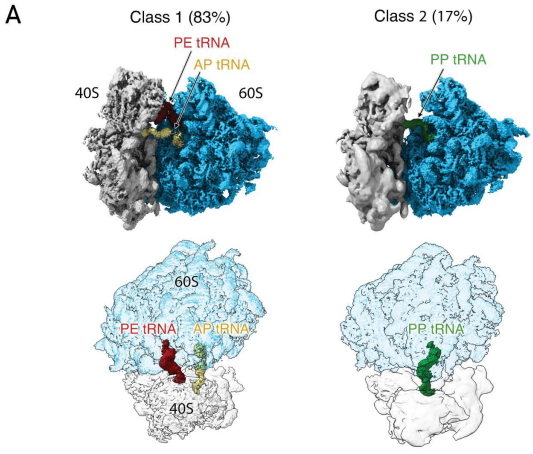
A
Class 1 (83%)
Class 2 (17%)
PE tRNA
AP tRNA
PP tRNA
40S
60S
60S
PE tRNA
AP tRNA
40S
PP tRNA

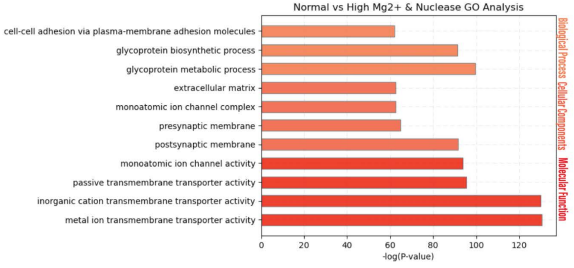
B
Normal vs High Mg2+ & Nuclease GO Analysis
cell-cell adhesion via plasma-membrane adhesion molecules
glycoprotein biosynthetic process
glycoprotein metabolic process
extracellular matrix
monoatomic ion channel complex
presynaptic membrane
postsynaptic membrane
monoatomic ion channel activity
passive transmembrane transporter activity
inorganic cation transmembrane transporter activity
metal ion transmembrane transporter activity
0
20
40
60
80
100
120
-log(P-value)
Biological Process
Cellular Components
Molecular Function

Figure 5

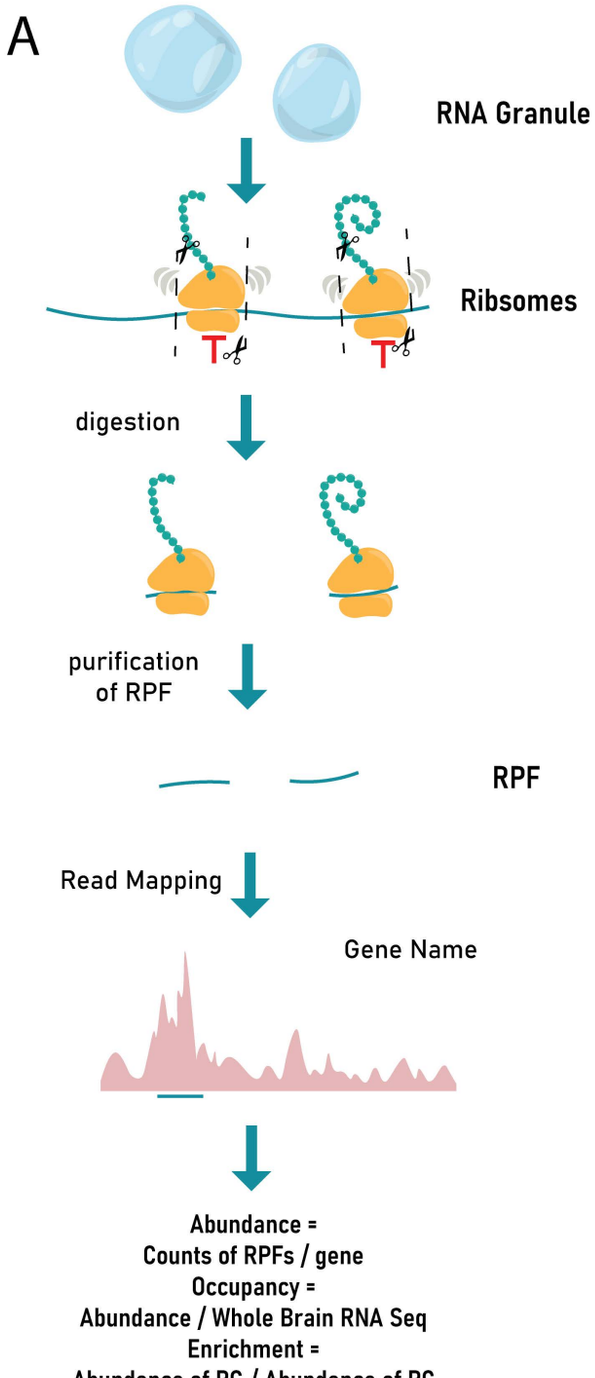
A
RNA Granule
Ribsomes
digestion
purification of RPF
RPF
Read Mapping
Gene Name
Abundance =
Counts of RPFs / gene
Occupancy =
Abundance / Whole Brain RNA Seq
Enrichment =
Abundance of RG / Abundance of RC

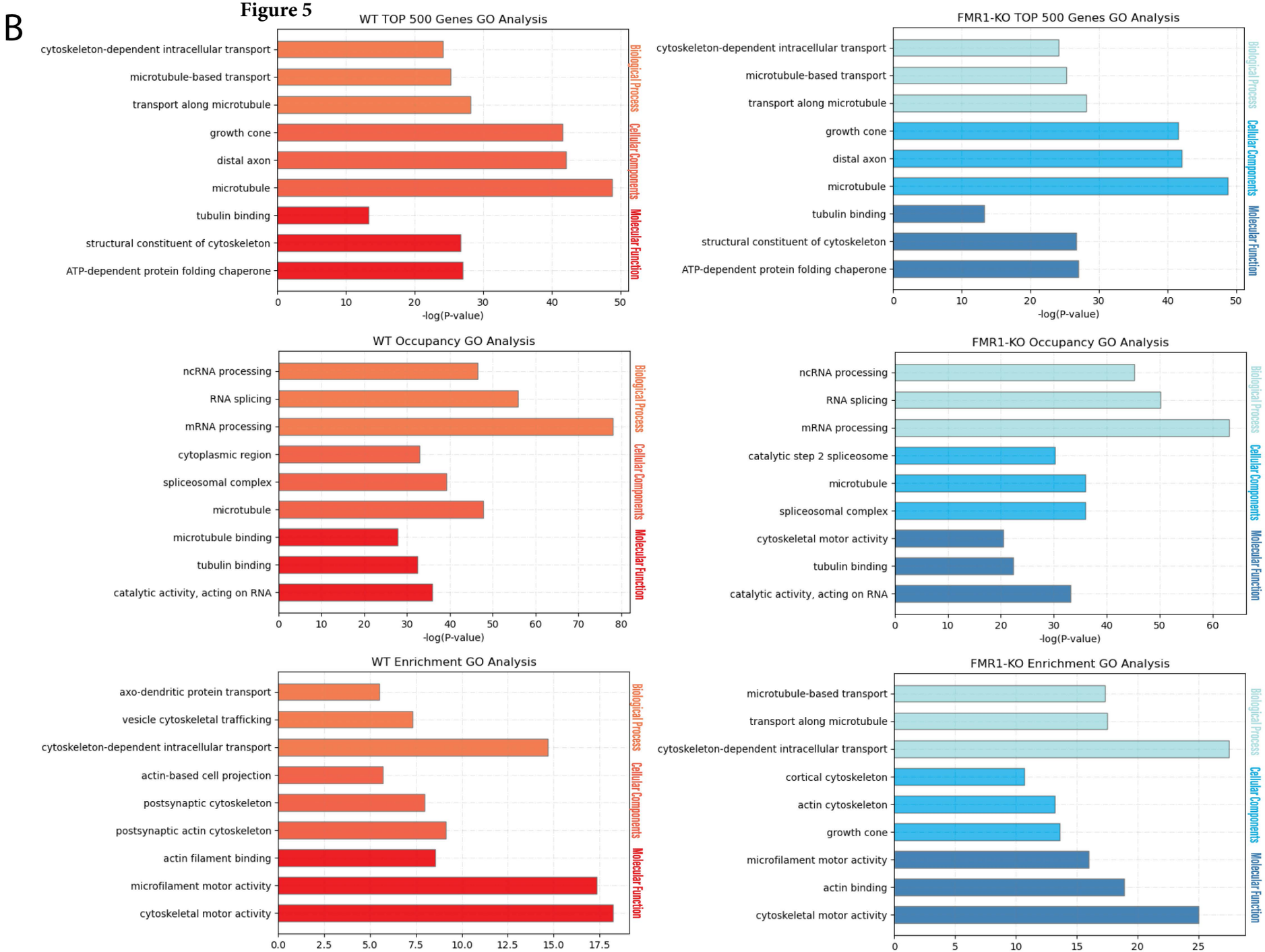
B
WT TOP 500 Genes GO Analysis
cytoskeleton-dependent intracellular transport
microtubule-based transport
transport along microtubule
growth cone
distal axon
microtubule
tubulin binding
structural constituent of cytoskeleton
ATP-dependent protein folding chaperone
-log(P-value)
FMR1-KO TOP 500 Genes GO Analysis
WT Occupancy GO Analysis
ncRNA processing
RNA splicing
mRNA processing
cytoplasmic region
spliceosomal complex
microtubule
microtubule binding
tubulin binding
catalytic activity, acting on RNA
FMR1-KO Occupancy GO Analysis
catalytic step 2 spliceosome
WT Enrichment GO Analysis
axo-dendritic protein transport
vesicle cytoskeletal trafficking
actin-based cell projection
postsynaptic cytoskeleton
postsynaptic actin cytoskeleton
actin filament binding
microfilament motor activity
cytoskeletal motor activity
FMR1-KO Enrichment GO Analysis
cortical cytoskeleton
actin cytoskeleton
actin binding
Biological Process
Cellular Components
Molecular Function

Figure 6

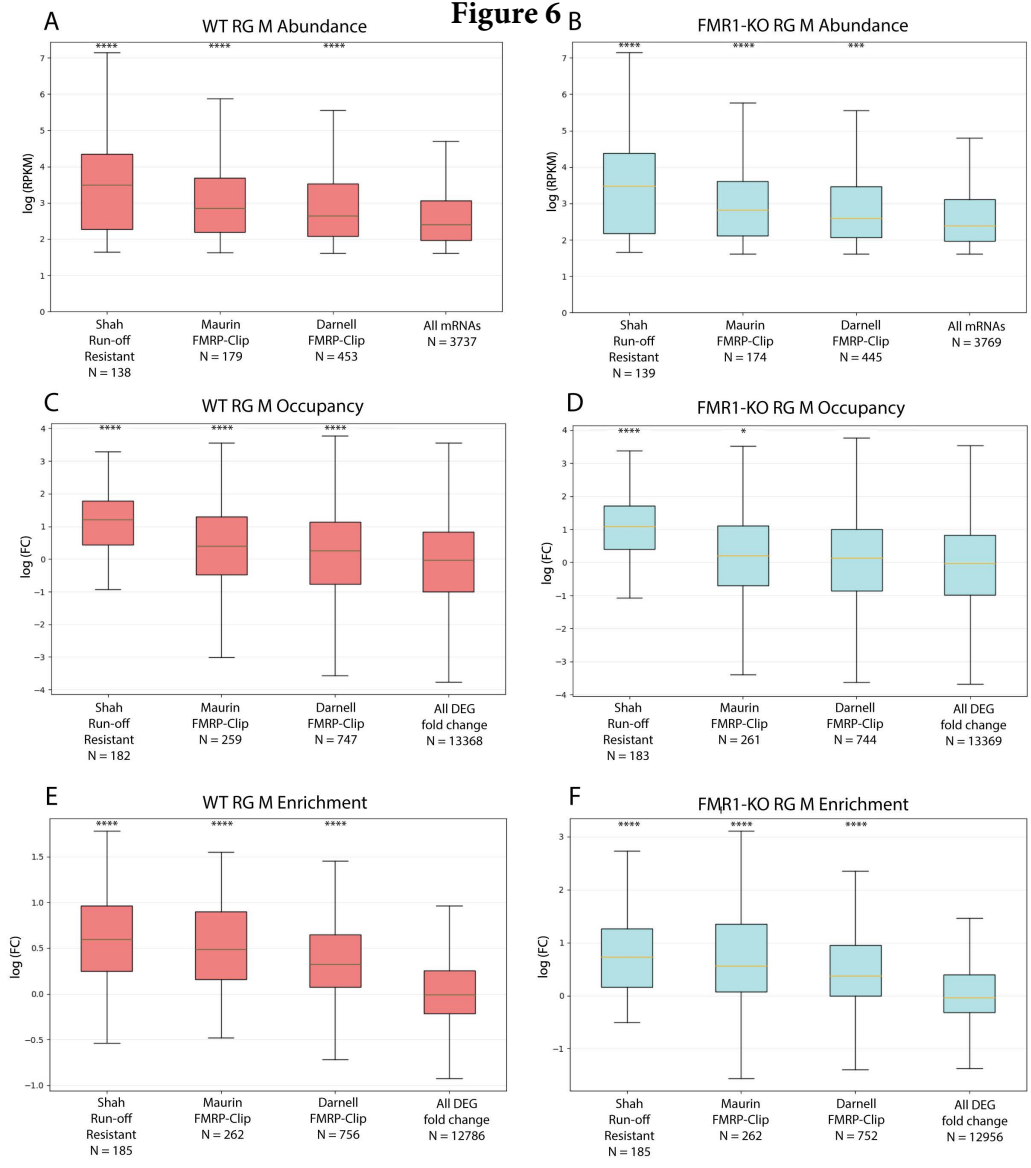
A
WT RG M Abundance
log (RPKM)
Shah Run-off Resistant N = 138
Maurin FMRP-Clip N = 179
Darnell FMRP-Clip N = 453
All mRNAs N = 3737
B
FMR1-KO RG M Abundance
log (RPKM)
Shah Run-off Resistant N = 139
Maurin FMRP-Clip N = 174
Darnell FMRP-Clip N = 445
All mRNAs N = 3769
C
WT RG M Occupancy
log (FC)
Shah Run-off Resistant N = 182
Maurin FMRP-Clip N = 259
Darnell FMRP-Clip N = 747
All DEG fold change N = 13368
D
FMR1-KO RG M Occupancy
log (FC)
Shah Run-off Resistant N = 183
Maurin FMRP-Clip N = 261
Darnell FMRP-Clip N = 744
All DEG fold change N = 13369
E
WT RG M Enrichment
log (FC)
Shah Run-off Resistant N = 185
Maurin FMRP-Clip N = 262
Darnell FMRP-Clip N = 756
All DEG fold change N = 12786
F
FMR1-KO RG M Enrichment
log (FC)
Shah Run-off Resistant N = 185
Maurin FMRP-Clip N = 262
Darnell FMRP-Clip N = 752
All DEG fold change N = 12956

Figure 7

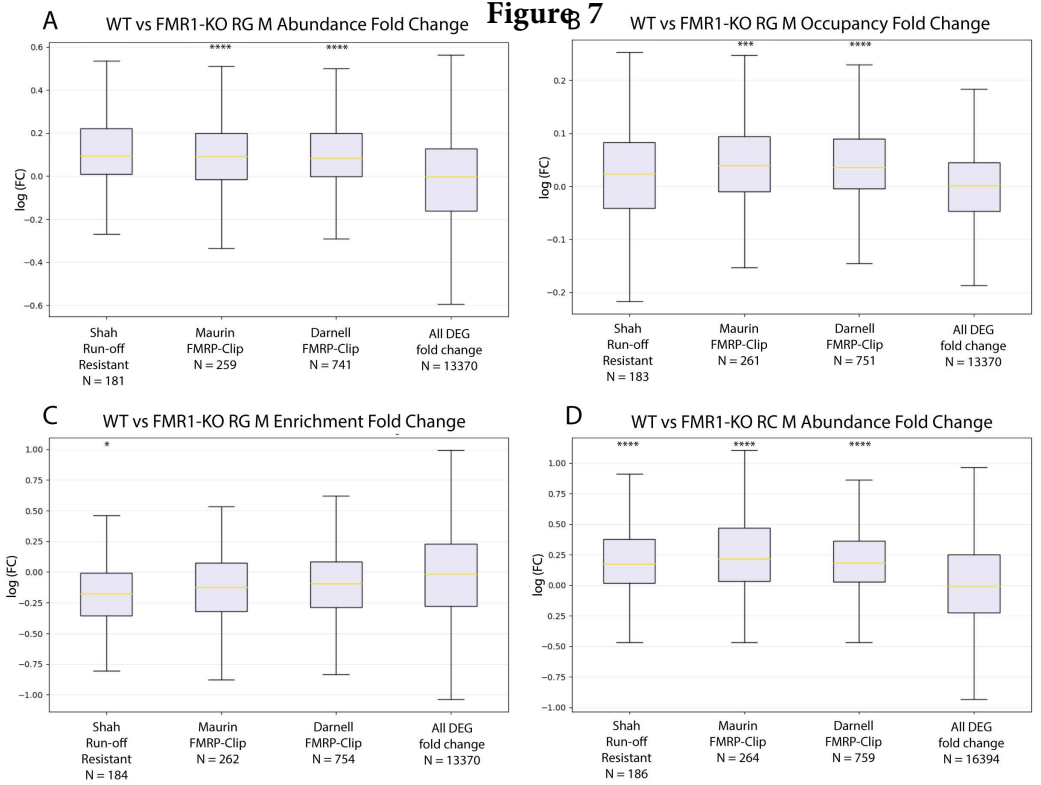
A
WT vs FMR1-KO RG M Abundance Fold Change
log (FC)
****
****
Shah Run-off Resistant N = 181
Maurin FMRP-Clip N = 259
Darnell FMRP-Clip N = 741
All DEG fold change N = 13370
B
WT vs FMR1-KO RG M Occupancy Fold Change
log (FC)
***
****
Shah Run-off Resistant N = 183
Maurin FMRP-Clip N = 261
Darnell FMRP-Clip N = 751
All DEG fold change N = 13370
C
WT vs FMR1-KO RG M Enrichment Fold Change
log (FC)
*
Shah Run-off Resistant N = 184
Maurin FMRP-Clip N = 262
Darnell FMRP-Clip N = 754
All DEG fold change N = 13370
D
WT vs FMR1-KO RC M Abundance Fold Change
log (FC)
****
****
****
Shah Run-off Resistant N = 186
Maurin FMRP-Clip N = 264
Darnell FMRP-Clip N = 759
All DEG fold change N = 16394

Figure 8

A

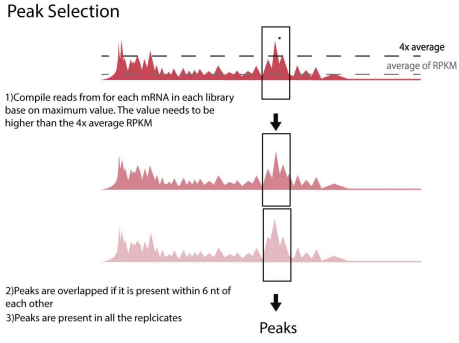

B

Sample	WT only	FMR1-KO only	All Sample
Number of Peaks	317	225	1392
% of Peaks w/ FXS Related Motif	64.0	60.9	66.5
Asp (D) Enrichment	1.89	1.79	2.01
Glu (E) Enrichment	1.48	2.01	1.59

C

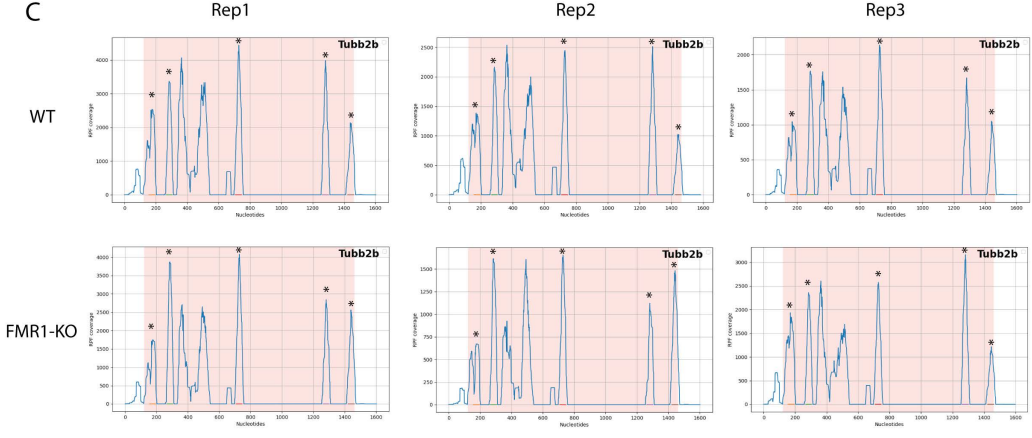

Figure 9

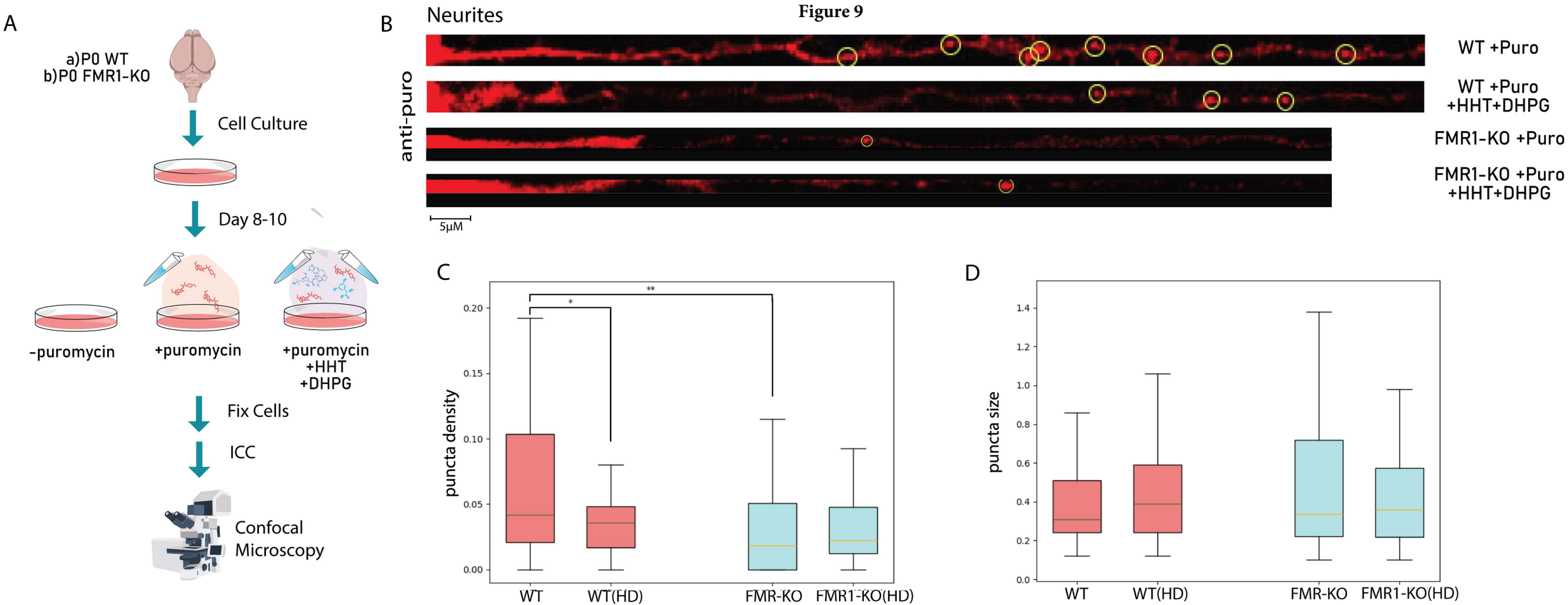
A
a)P0 WT
b)P0 FMR1-KO
Cell Culture
Day 8-10
-puromycin
+puromycin
+puromycin
+HHT
+DHPG
Fix Cells
ICC
Confocal
Microscopy
B
Neurites
anti-puro
5μM
WT +Puro
WT +Puro
+HHT+DHPG
FMR1-KO +Puro
FMR1-KO +Puro
+HHT+DHPG
C
puncta density
0.00
0.05
0.10
0.15
0.20
*
**
WT
WT(HD)
FMR-KO
FMR1-KO(HD)
D
puncta size
0.0
0.2
0.4
0.6
0.8
1.0
1.2
1.4
WT
WT(HD)
FMR-KO
FMR1-KO(HD)

Figure S3-1

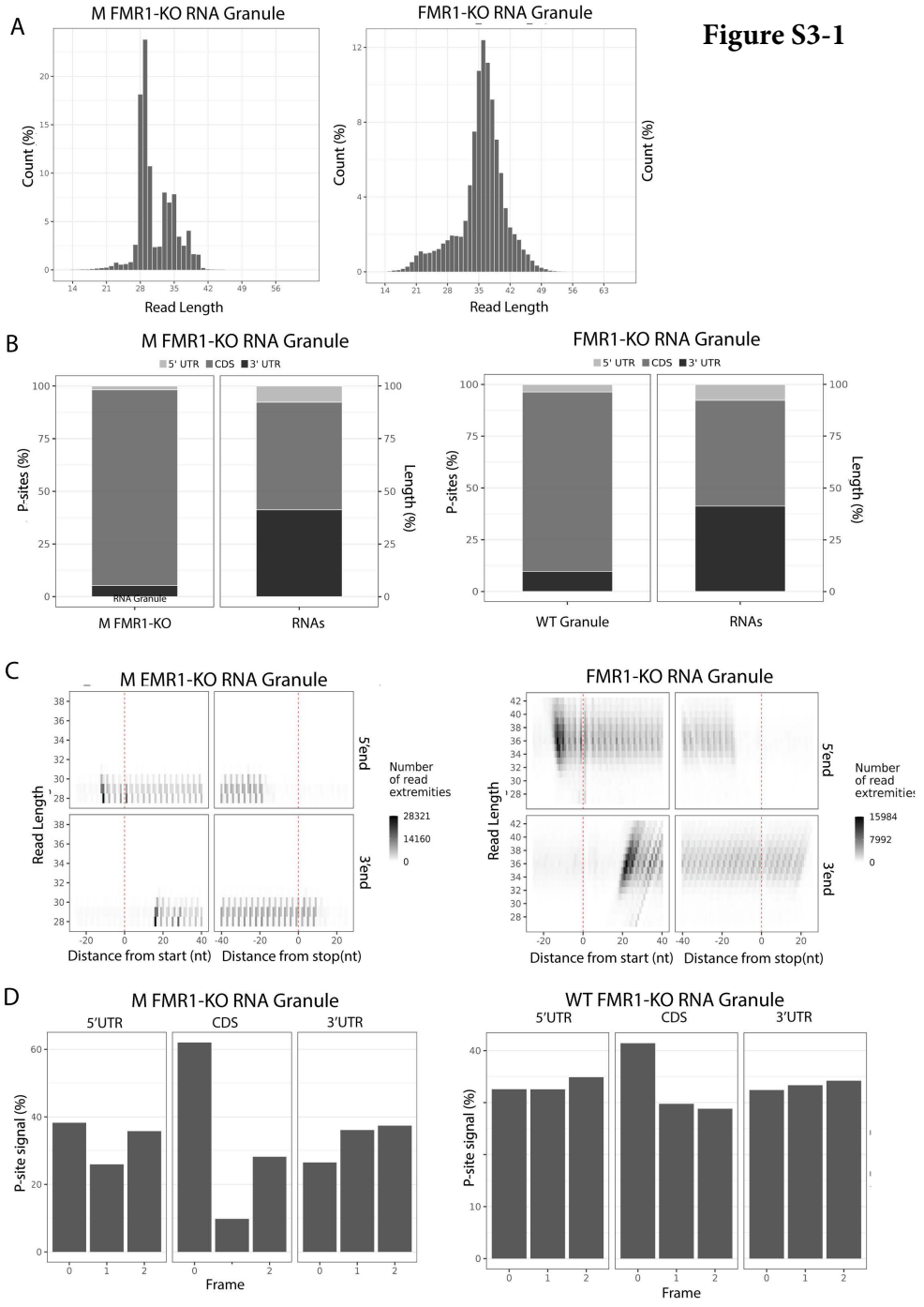
A
M FMR1-KO RNA Granule
FMR1-KO RNA Granule
Count (%)
Read Length
B
M FMR1-KO RNA Granule
FMR1-KO RNA Granule
5' UTR
CDS
3' UTR
P-sites (%)
Length (%)
RNA Granule
M FMR1-KO
RNAs
WT Granule
C
M EMR1-KO RNA Granule
FMR1-KO RNA Granule
Read Length
5'end
3'end
Number of read extremities
28321
14160
0
15984
7992
Distance from start (nt)
Distance from stop(nt)
D
M FMR1-KO RNA Granule
WT FMR1-KO RNA Granule
5'UTR
CDS
3'UTR
P-site signal (%)
Frame

Figure S3-2

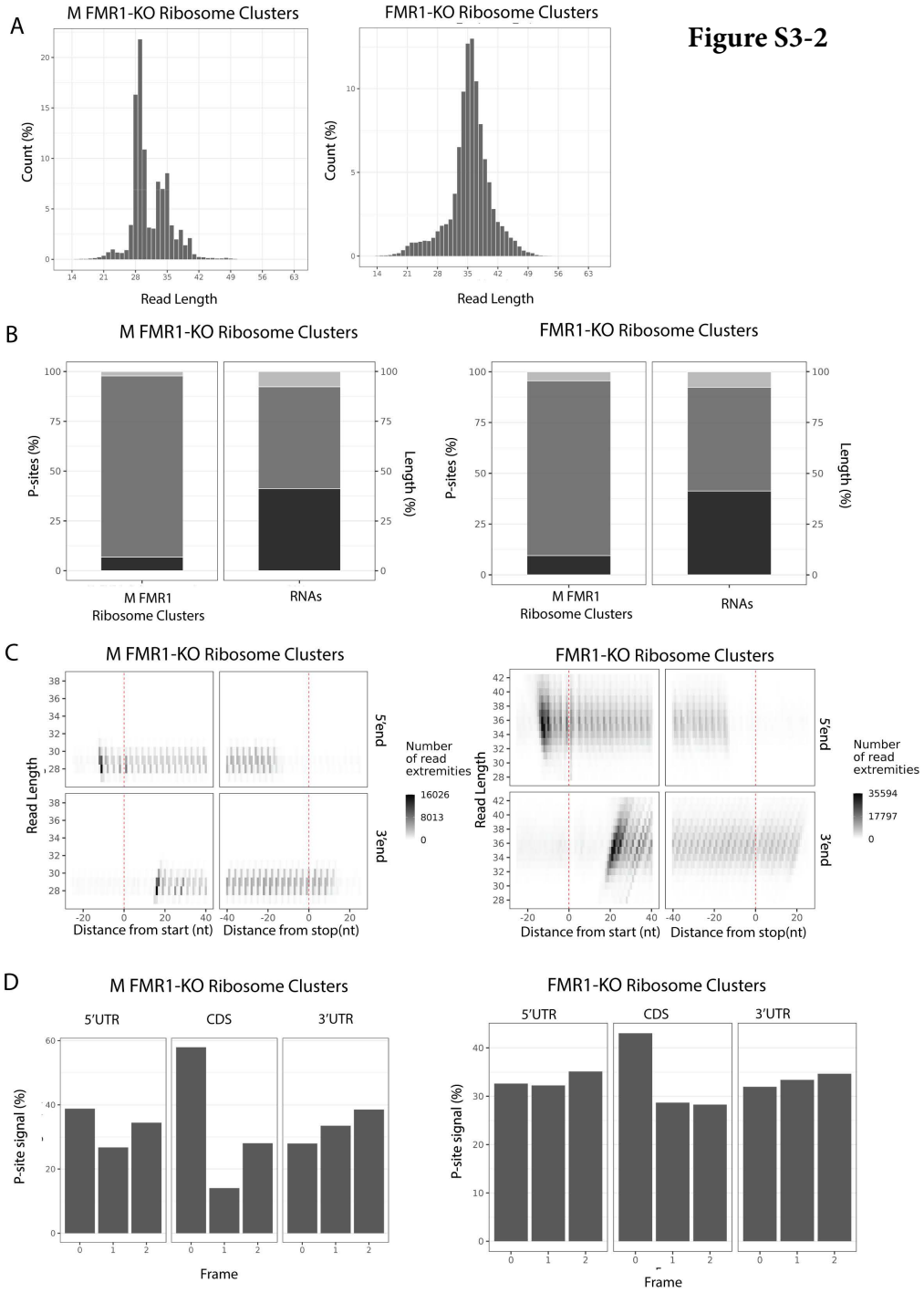
A
M FMR1-KO Ribosome Clusters
FMR1-KO Ribosome Clusters
Count (%)
Read Length
B
M FMR1-KO Ribosome Clusters
FMR1-KO Ribosome Clusters
P-sites (%)
Length (%)
M FMR1
Ribosome Clusters
RNAs
C
M FMR1-KO Ribosome Clusters
FMR1-KO Ribosome Clusters
Read Length
5'end
3'end
Number
of read
extremities
16026
8013
0
35594
17797
0
Distance from start (nt)
Distance from stop(nt)
D
M FMR1-KO Ribosome Clusters
FMR1-KO Ribosome Clusters
5'UTR
CDS
3'UTR
P-site signal (%)
Frame

Figure S3-3

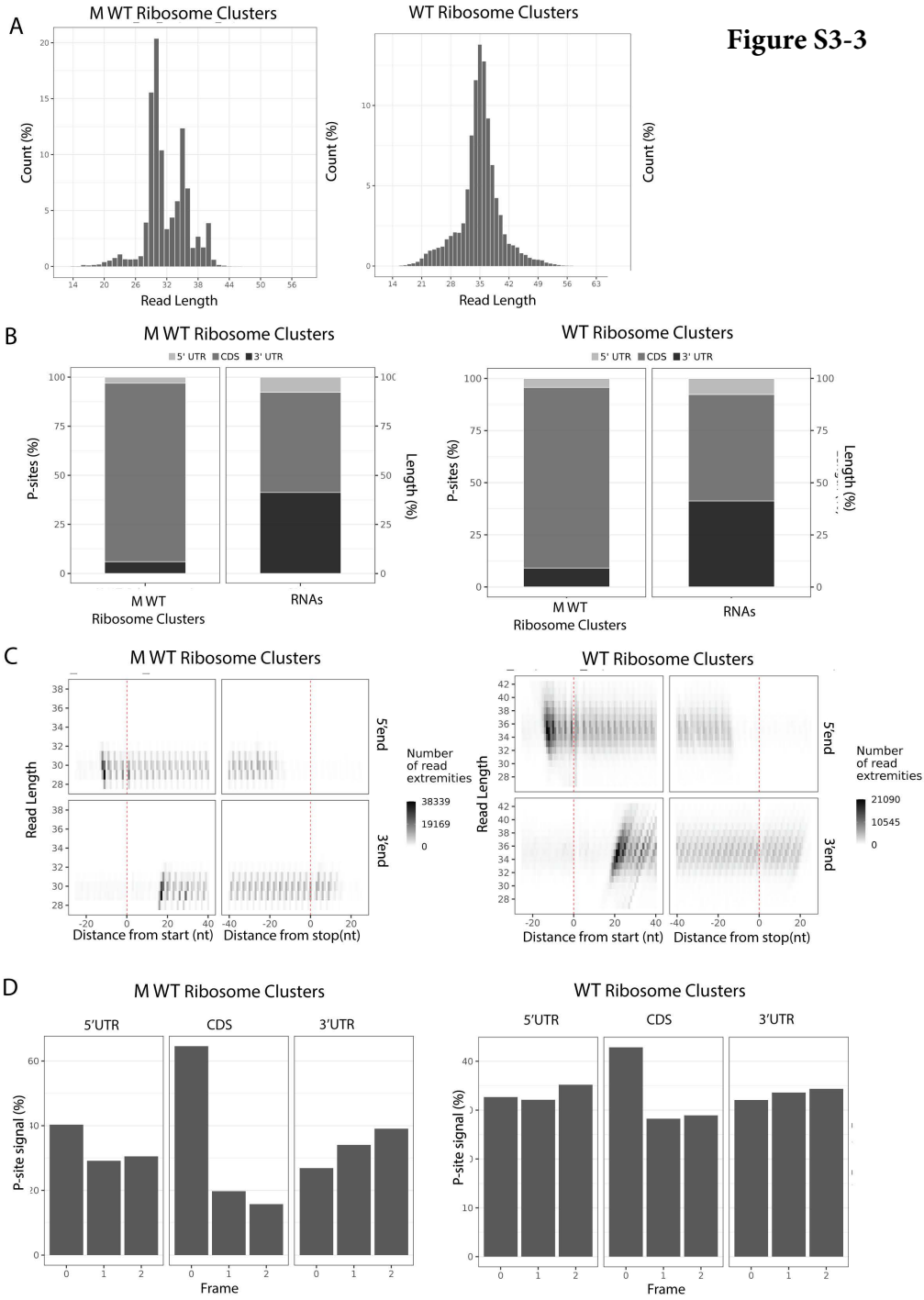
A
M WT Ribosome Clusters
WT Ribosome Clusters
Count (%)
Read Length
B
M WT Ribosome Clusters
WT Ribosome Clusters
5' UTR CDS 3' UTR
P-sites (%)
Length (%)
M WT
Ribosome Clusters
RNAs
C
M WT Ribosome Clusters
WT Ribosome Clusters
Read Length
5'end
3'end
Number of read extremities
38339
19169
0
21090
10545
Distance from start (nt)
Distance from stop(nt)
D
M WT Ribosome Clusters
WT Ribosome Clusters
5'UTR
CDS
3'UTR
P-site signal (%)
Frame

Figure S4-1

All movies (10,866)

↓

Patch motion correction

↓

Patch CTF estimation

↓

Particle picking
(Blob picker + Template picker + Topaz)

↓

Particle curation step 1:
2D Classification (2 cycles)

↓

Particle curation step 2:
Ab initio Reconstruction + Heterogeneous refinement
(890,644 particles)

↓

Non-Uniform Refinement

↓

3D Variability Analysis + 3D Variability Display
(2 rounds)

Class 1. 80S with AP and PE tRNA
(83%)

Class 2. 80S with PP tRNA
(17%)

Non-Uniform Refinement

Consensus map class 1 (2.8 Å)

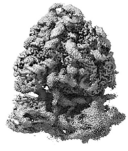

Consensus map class 2 (3.2 Å)

Particle subtraction
+ Local Refinement

60S (2.7 Å)

40S (3.3 Å)

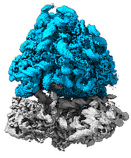

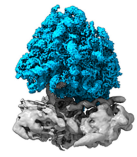

60S (3.2 Å)

40S (4.5 Å)

Figure S4-2

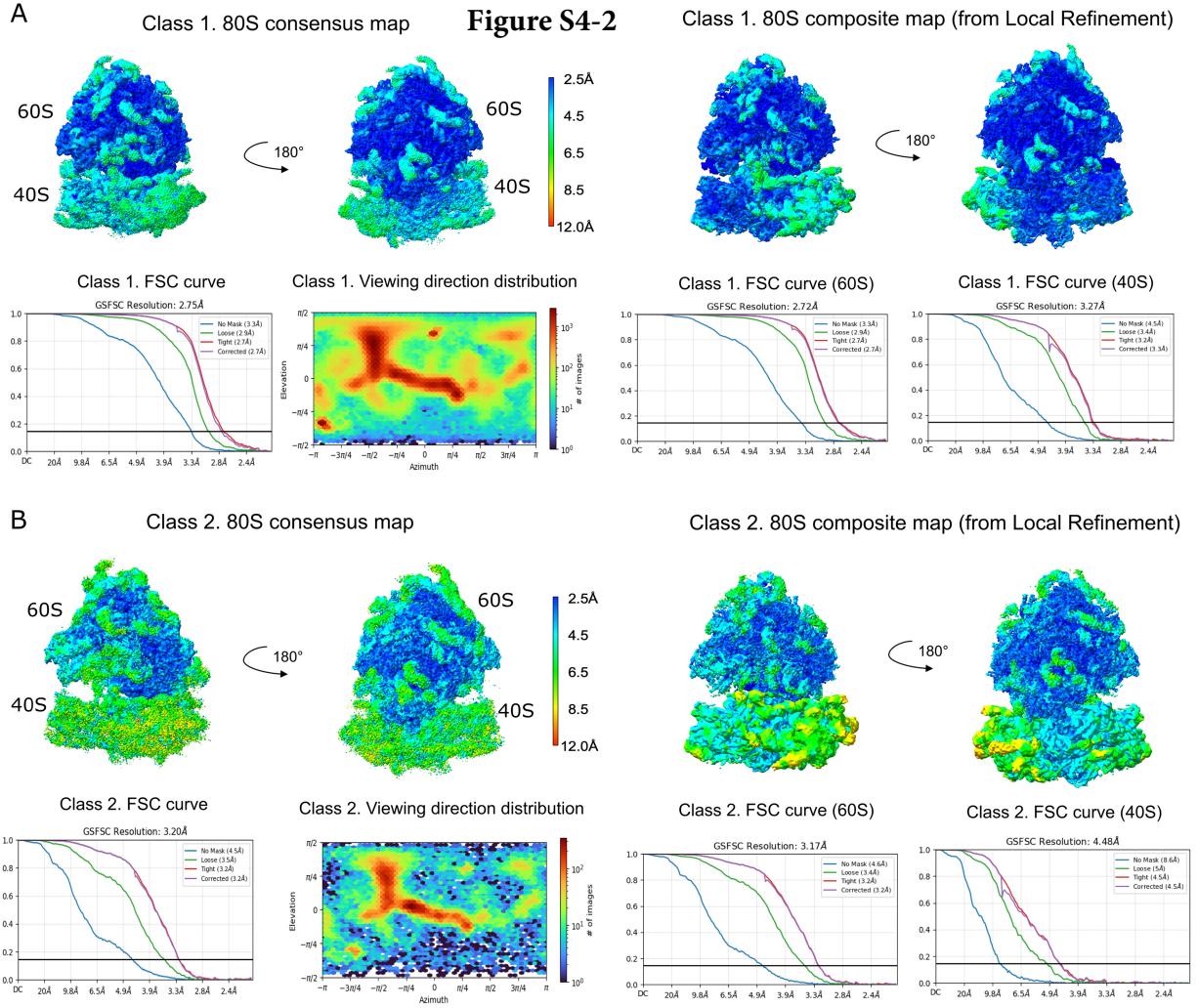
A
Class 1. 80S consensus map
60S
40S
180°
60S
40S
2.5Å
4.5
6.5
8.5
12.0Å
Class 1. 80S composite map (from Local Refinement)
180°
Class 1. FSC curve
GSFSC Resolution: 2.75Å
No Mask (3.3Å)
Loose (2.9Å)
Tight (2.7Å)
Corrected (2.7Å)
Class 1. Viewing direction distribution
Elevation
Azimuth
# of images
Class 1. FSC curve (60S)
GSFSC Resolution: 2.72Å
No Mask (3.3Å)
Loose (2.9Å)
Tight (2.7Å)
Corrected (2.7Å)
Class 1. FSC curve (40S)
GSFSC Resolution: 3.27Å
No Mask (4.5Å)
Loose (3.4Å)
Tight (3.2Å)
Corrected (3.3Å)
B
Class 2. 80S consensus map
60S
40S
180°
60S
40S
2.5Å
4.5
6.5
8.5
12.0Å
Class 2. 80S composite map (from Local Refinement)
180°
Class 2. FSC curve
GSFSC Resolution: 3.20Å
No Mask (4.5Å)
Loose (3.5Å)
Tight (3.2Å)
Corrected (3.2Å)
Class 2. Viewing direction distribution
Elevation
Azimuth
# of images
Class 2. FSC curve (60S)
GSFSC Resolution: 3.17Å
No Mask (4.6Å)
Loose (3.4Å)
Tight (3.2Å)
Corrected (3.2Å)
Class 2. FSC curve (40S)
GSFSC Resolution: 4.48Å
No Mask (8.6Å)
Loose (5Å)
Tight (4.5Å)
Corrected (4.5Å)

Figure S8-1

A

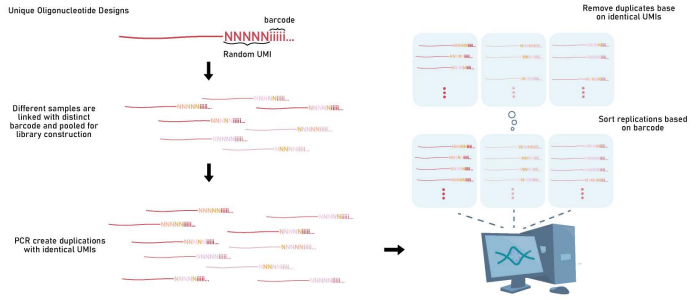

B

	WT	FMR1-KO
% duplication in Rep1	65.7	70.5
% duplication in Rep2	57.2	61.3
% duplication in Rep3	59.2	61.5

C

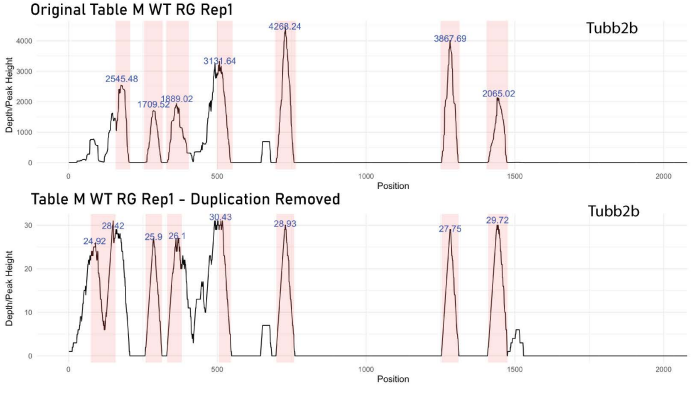

D

Sample	WT only	FMR1-KO only	All Sample
Number of Peaks	181	125	615
% of Peaks w/ FXS Related Motif	74.6	80.0	74.1
Asp (D) Enrichment	2.13	2.06	2.42
Glu (E) Enrichment	1.75	1.70	2.07

Figure S9-1

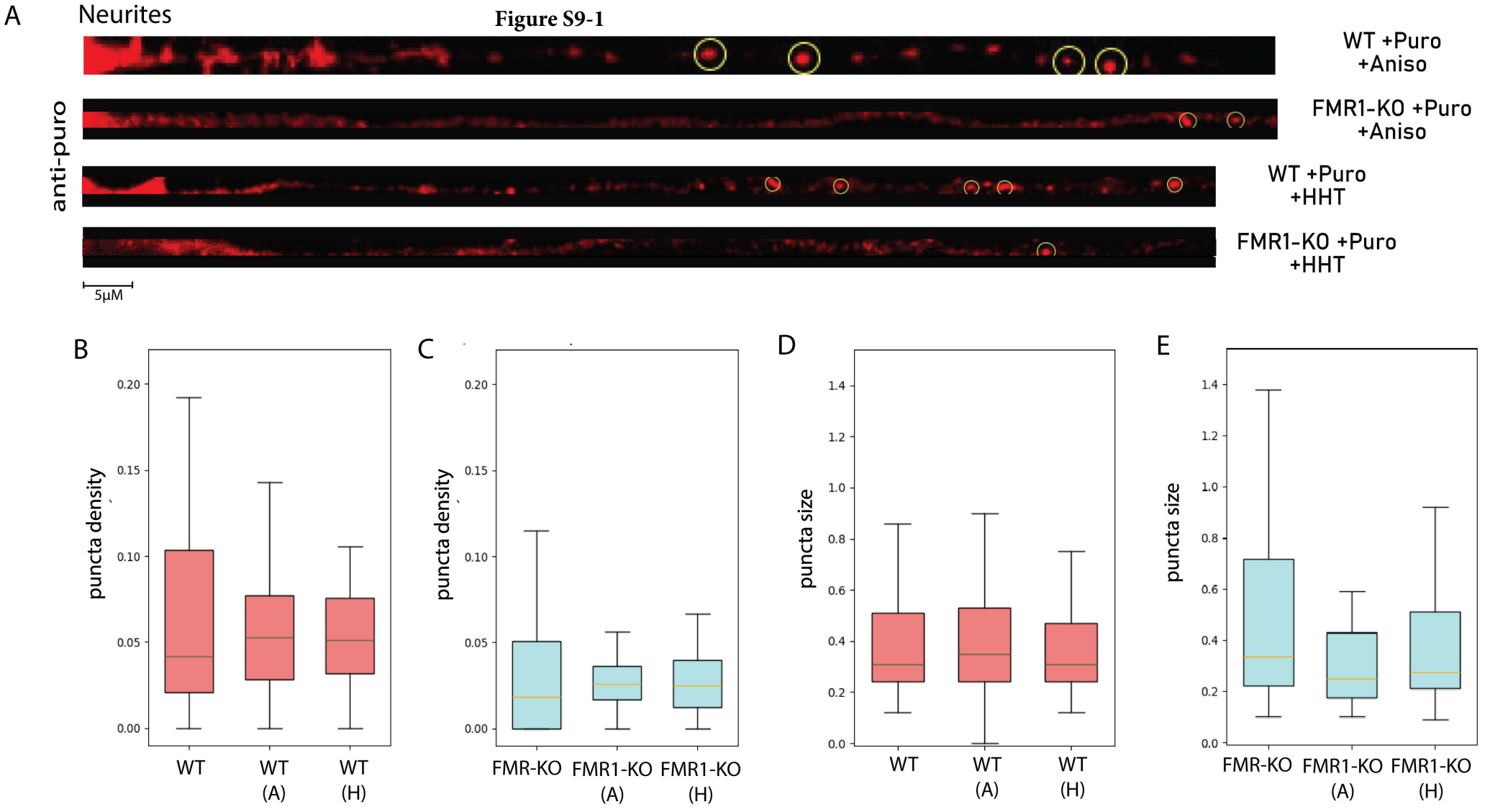
A
Neurites
anti-puro
WT +Puro +Aniso
FMR1-KO +Puro +Aniso
WT +Puro +HHT
FMR1-KO +Puro +HHT
5μM
B
puncta density
0.20
0.15
0.10
0.05
0.00
WT
WT (A)
WT (H)
C
puncta density
0.20
0.15
0.10
0.05
0.00
FMR-KO
FMR1-KO (A)
FMR1-KO (H)
D
puncta size
1.4
1.2
1.0
0.8
0.6
0.4
0.2
0.0
WT
WT (A)
WT (H)
E
puncta size
1.4
1.2
1.0
0.8
0.6
0.4
0.2
0.0
FMR-KO
FMR1-KO (A)
FMR1-KO (H)